HHS Public Access

Author manuscript

Nat Neurosci. Author manuscript; available in PMC 2019 December 24.

Pericyte loss leads to circulatory failure and pleiotrophin depletion causing neuron loss

Angeliki M. Nikolakopoulou[1,2,*], **Axel Montagne**[1,2,*], **Kassandra Kisler**[1,2,*], **Zhonghua Dai**[1,2,*], **Yaoming Wang**[1,2], **Mikko T. Huuskonen**[1,2], **Abhay P. Sagare**[1,2], **Divna Lazic**[1,2], **Melanie D. Sweeney**[1,2], **Pan Kong**[1,2], **Min Wang**[1,2], **Nelly Chuqui Owens**[1,2], **Erica J. Lawson**[1,2], **Xiaochun Xie**[1,2], **Zhen Zhao**[1,2,#], **Berislav V. Zlokovic**[1,2,#]

[1]Zilkha Neurogenetic Institute, Keck School of Medicine, University of Southern California, Los Angeles, CA 90089, USA.

[2]Department of Physiology and Neuroscience, Keck School of Medicine, University of Southern California, Los Angeles, CA 90089, USA.

Abstract

Pericytes are positioned between brain capillary endothelial cells, astrocytes and neurons. They degenerate in multiple neurological disorders. However, their role in the pathogenesis of these disorders remains debatable. Here, we generated an inducible pericyte-specific Cre line and crossed pericyte-specific Cre mice with iDTR mice carrying Cre-dependent human diphtheria toxin receptor (DTR). After pericyte ablation with diphtheria toxin, mice developed an acute blood-brain barrier (BBB) breakdown, severe loss of blood flow, and a rapid neuron loss associated with loss of pericyte-derived pleiotrophin (PTN), a neurotrophic growth factor. Intracerebroventricular PTN infusions prevented neuron loss in pericyte-ablated mice despite persistent circulatory changes. Silencing pericyte-derived *Ptn* rendered neurons vulnerable to ischemic and excitotoxic injury. Our data demonstrate a rapid neurodegeneration cascade linking pericyte loss to acute circulatory collapse and loss of PTN neurotrophic support. These findings could have implications for the pathogenesis and treatment of neurological disorders associated with pericyte loss and/or neurovascular dysfunction.

Address correspondence: Berislav V. Zlokovic, M.D., Ph.D., Zilkha Neurogenetic Institute, 1501 San Pablo Street, Los Angeles, CA 90089, Phone: 323.442.2722 / Fax: 323.666.2184, zlokovic@usc.edu.
*Equally contributed first co-authors
#Senior co-authors

Competing Interest Statement
The authors declare no competing interests.

INTRODUCTION

Pericytes are vascular mural cells embedded in the basement membrane of brain capillaries[1,2]. They extend their processes to the neighboring brain capillaries, pre-capillary arterioles and post-capillary venules. In the central nervous system (CNS), pericytes are positioned centrally within the neurovascular unit between brain capillary endothelial cells that form the blood-brain barrier (BBB), astrocytes and neurons[2]. They play a key role in signaling within the neurovascular unit at the brain capillary level and regulate multiple neurovascular functions. This includes angiogenesis during CNS development[3], BBB permeability in the developing and adult CNS[4–6], clearance of toxic metabolites[7–9], blood flow responses[10–13], inflammatory responses and stem cell activity[2].

Pericyte loss is found in both acute and chronic CNS disorders[14]. They rapidly die after ischemic stroke[11] and brain trauma[15] and degenerate in cerebral autosomal dominant arteriopathy with subcortical infarcts and leukoencephalopathy (CADASIL), the most common genetic form of stroke[16]. Massive regional loss of pericytes was shown in Alzheimer's disease[1,14,17,18], amyotrophic lateral sclerosis (ALS)[19], human immunodeficiency virus (HIV)-associated neurocognitive disorder[20], Parkinson's disease and Huntington's disease, as recently reviewed[1,14]. However, their role in the pathogenesis of these acute and chronic CNS disorders remains still debatable.

One of the key obstacles in better understanding the role of CNS pericytes is lack of pericyte-specific models including pericyte-specific Cre line and pericyte-specific ablation models. To overcome this difficulty, here, we generated an inducible pericyte-specific Cre line utilizing a double-promoter approach with the platelet-derived growth factor receptor-β (*Pdgfrb*)[21] and chondroitin sulfate proteoglycan-4 (*Cspg4*)[22] promoters. To ablate pericytes without affecting other brain cell types, we crossed pericyte-specific Cre mice with the iDTR mice carrying Cre-dependent human diphtheria toxin receptor (DTR)[23]. We then ablated pericytes with diphtheria toxin, and studied the link between pericyte loss and neuron loss and/or degeneration.

RESULTS

Generation of pericyte-specific Cre line

The canonical markers of brain pericytes are typically shared with other brain cell types[2]. Therefore, to generate pericyte-specific line we employed a double promoter strategy using both *Pdgfrb*[21] and *Cspg4*[22] promoters. We hypothesized that combining these two promoters that drive expression of *Pdgfrb*[21] and *Cspg4*[22] genes enriched in pericytes relative to other brain cell types[24–27] (Supplementary Fig. 1a–d), will focus Cre recombinase expression to pericytes (Supplementary Fig. 1e). We made two constructs: one expressing Flippase (Flp) recombinase under the control of *Pdgfrβ* promoter, and the other carrying a *Frt-Stop-Frt-CreER* cassette (*Frt*: flippase recognition target; *CreER:* recombinant protein between Cre recombinase and a mutated ligand binding domain of the estrogen receptor[28]) under the control of *Cspg4* promoter (Fig. 1a, **left**). Initially, we tested cell specificity of the two-promoter strategy in primary mouse brain endothelial cells, pericytes and vascular smooth cells (VSMCs). After co-transfection with *Cspg4-FSF-CreER*, *Pdgfrβ-Flp* and a Cre-

dependent green fluorescent protein (GFP) reporter the only cell type that allowed for both Flp and CreER expression resulting in GFP expression were pericytes (Supplementary Fig. 1f,g).

Next, we generated *Pdgfrβ-Flp; Cspg4-FSF-CreER* mice by co-injecting both linearized constructs into C57BL/6 blastocysts (Fig. 1a, *left*). To characterize Cre expression, we crossed a line that stably carried *Pdgfrβ-Flp* and *Cspg4-FSF-CreER* cassettes (Supplementary Fig. 2a,b) with the Ai14 tdTomato reporter line[29] (Fig. 1a, *right*). Tamoxifen (TAM) treatment, led to tdTomato expression only in the mural cells on CD31+ endothelial brain capillary profiles (6 μm in diameter)[4,5], but not on larger arteriolar vessels (Fig. 1b,c) or mural α-smooth muscle actin (SMA)+ VSMCs of small arterioles[24] (Fig. 1d,e). tdTomato colocalized exclusively with CD13+ (Fig. 1f) or PDGFRβ+ (Supplementary Fig. 2c) pericytes[4,5], but not CD31+ endothelial cells (Fig. 1f). Olig2+ oligodendrocytes (Supplementary Fig. 2d), GFAP+ astrocytes (Supplementary Fig. 2e,f), NeuN+ neurons (Supplementary Fig. 2g), or ionized calcium binding adaptor molecule-1+ microglia (Supplementary Fig. 2h) did not express tdTomato. TAM treatment (40 mg/kg daily, 2, 4 and 7 injections) dose-dependently increased tdTomato expression in CD13+ pericytes (Fig. 1g,h), indicating we generated an inducible pericyte-specific Cre line. See Methods for more details on double promoter strategy.

Pericyte ablation with diphtheria toxin

To ablate pericytes, we crossed pericyte-CreER mice with iDTR mice carrying Cre-dependent human DTR[23], which leads to cell death after diphtheria toxin (DT) administration[23,30] (Fig. 2a). TAM treatment (40 mg/kg daily for 7 consecutive days), and DT treatment (0.1 μg daily for 10 consecutive days beginning 2 weeks after TAM) or vehicle, were modified from studies ablating DTR-expressing oligodendrocytes[23] and microglia[31] (Fig. 2b). All analyses were performed at 0, 3, 6 and 9 days of DT treatment, and 3 and 15 days post-DT treatment (Fig. 2b). TAM induced DTR expression in brain capillaries of pericyte-CreER; iDTR mice, and subsequent DT treatment depleted brain capillary DTR, which was associated with a loss of PDGFRβ, a pericyte marker[4,5,32], but not CD31, a brain endothelial marker[4,5,32], as shown by immunoblotting (Fig. 2c,d). Since brain capillaries did not contain SMA+ VSMCs[24] (Fig. 2c) these data suggested that DT was killing PDGFRβ+ pericytes. Tissue analysis confirmed progressive loss of tdTomato+ CD13+ pericytes on cortical and hippocampal capillaries (6 μm in diameter) from 35% (6 days of DT) to 95% and 100% at 3 and 15 days post-DT, respectively, compared to vehicle (Fig. 2e,f). This led to approximately 20%, 40%, and 60% loss of CD13+ pericytes[32] at 6 and 9 days of DT, and 3–15 days post DT, respectively (Fig. 2g), and the accompanying loss of CD13+ pericyte coverage (Fig. 2h,i). TUNEL staining further confirmed that DT was killing tdTomato+ CD13+ pericytes (Fig. 2j,k).

Consistent with lack of tdTomato expression in SMA+ VSMCs (Fig. 1b–e), DT did not ablate VSMCs in TAM-treated pericyte-CreER; iDTR mice as shown by no change in the thickness of VSMCs-covered arteriolar wall (Fig. 2l,m), number of VSMCs (Fig. 2n), and/or cerebral blood flow (CBF) response to adenosine, an endothelium-independent VSMCs

relaxant[13] (Fig. 2o), suggesting intact VSMCs function. DT also did not ablate astrocytes, microglia or oligodendrocytes (Supplementary Fig. 3a–d).

Acute circulatory failure after pericyte ablation

To determine whether pericyte loss affects CBF, we employed a longitudinal dynamic susceptibility-contrast (DSC)-magnetic resonance imaging (MRI) with gadolinium, which generates regional CBF values in mice comparable to values generated by a 'gold-standard' ^{14}C-iodoantipyrine autoradiography[8]. DSC-MRI revealed CBF loss in the cortex and hippocampus of TAM-treated pericyte-CreER; iDTR mice beginning at day 9 of DT, followed by 50% CBF reductions at 3 and 15 days post-DT (Fig. 3a,b), which has been independently confirmed with an iron oxide contrast agent (Supplementary Fig. 4a).

The BBB unidirectional transfer constant, K_{trans}, maps to gadolinium generated by a longitudinal dynamic contrast-enhanced (DCE)-MRI[8], indicated BBB breakdown in the cortex and hippocampus of TAM-treated pericyte-CreER; iDTR mice, beginning at 6 days of DT (corresponding to first detectable ~20% loss of pericytes) and advancing to >60% increase in the K_{trans} values compared to vehicle at 3 and 15 days post-DT (Fig. 3c,d), corresponding to 60% loss of pericytes. Tissue analysis of perivascular immunoglobulin G (Fig. 3e,f) and fibrinogen (Supplementary Fig. 4b,c) deposits confirmed BBB breakdown that was most pronounced in vessels lacking pericyte coverage (Supplementary Fig. 4d).

Consistent with BBB breakdown, the length of the tight junction proteins zonula occludens and occludin, and the adherens junction protein VE-cadherin[1] on cortical and hippocampal capillaries of TAM-treated pericyte-CreER; iDTR mice was reduced by 50–60% at 3 days post-DT (Supplementary Fig. 4e–j), which has been confirmed by immunoblotting of brain capillaries (Supplementary Fig. 4k,l). Electron microscopy analysis did not show evidence of enhanced transcytosis (Supplementary Fig. 4m,n).

To explore possible mechanisms of circulatory failure we studied whether pericyte cell death leads to "rigor mortis" hypercontractile state of dying pericytes, as shown after stroke[11]. Cell death and contractility measurements of DTR-expressing mouse pericytes indicated, however, that pericytes do not contract when killed by toxin (Supplementary Fig. 5a,b; Supplementary videos 1–3). Leukocytes plugging and platelets accumulation (thrombosis of vessels) also did not contribute to blood flow obstructions (Supplementary Fig. 5c). But, diffusion MRI revealed development of vasogenic edema, as shown by 15–18% and >20% increase in the tissue apparent diffusion coefficient (ADC) at day 9 of DT and 15 days post-DT compared to vehicle (Supplementary Fig. 5d–f). The edema was somewhat less pronounced than after ischemic stroke (Supplementary Fig. 5g), and was driven by an early BBB breakdown (Fig. 3c–f; Supplementary Fig. 5h–i). Consistent with tissue swelling, we found reduced red blood cells flow and a decrease in capillary diameters (Supplementary Fig. 5j–l) and reduced CBF (Fig. 3a,b), which led to tissue hypoxia (Supplementary Fig. 5m,n) and accumulation of neurotoxic glutamate in the cerebrospinal fluid (CSF) at levels comparable to those as seen after ischemic stroke (Supplementary Fig. 5o).

In contrast to BBB breakdown (Fig. 3c–f), edema (Supplementary Fig. 5d–g) and CBF reductions (Fig. 3a,b) after global pericyte loss, ablating single pericytes decreases flow

resistance and dilates capillaries, but does not disrupt the BBB[33] and/or lead to edema likely due to compensatory influences from non-ablated neighboring pericytes[2]. Although pericytes establish the blood-retinal barrier (BRB)[34,35], one study suggested they are not required for the maintenance of the adult BRB[34]. However, other studies suggested that pericytes maintain the adult BRB[35] and BBB[4,5] as confirmed with the present findings.

Pericytes in peripheral organs (e.g., kidney, liver, heart) were only sparsely labeled in the present model (Supplementary Fig. 6a–d) consistent with the concept that peripheral pericytes differ from brain pericytes and may have a different origin[24,27]. For example, in the kidney, <5% of PDGFRβ+ pericytes express NG2[36,37]. As the present model requires both genes to be expressed in the cell at the same time, it is not surprising that peripheral pericytes in the kidney have not been affected. Additionally, we showed that ablation of brain pericytes did not affect systemic physiological and biochemical parameters, liver and kidney analyses (Supplementary Fig. 6e–g) or visual perception (acuity) (Supplementary Fig. 6h).

Rapid neuron loss after pericyte ablation

Unexpectedly, we found rapid loss of neurons and behavioral deficits within days of pericyte ablation, as shown by 20–25% loss of NeuN+ neurons and 35–40% loss of SMI312+ neuritic density in cortex and hippocampus (Fig. 3g–i) accompanied by poor performance on novel object location and fear conditioning tests as shown 15 days post-DT (Fig. 3j,k). In the absence of DTR-expressing pericytes, control iDTR mice treated with TAM and DT, or pericyte-CreER; iDTR mice treated with TAM and vehicle, did not show circulatory (Supplementary Fig. 7a–g), neuronal (Supplementary Fig. 7h–j) or behavior (Supplementary Fig. 7k,l) changes.

Loss of pericyte-derived pleiotrophin-mediated neuroprotection

To address why pericyte ablation leads to rapid neuron loss, we next asked whether rapid pericyte loss deprives neurons of pericyte-derived neurotrophic support. We focused on pleiotrophin (PTN), a pericyte-secreted growth factor expressed in the brain, but not in peripheral organs[38], whose expression is enriched in pericytes compared to other brain cell types[5,24,39], and/or other growth factors secreted by pericytes[24]. Using dual fluorescent *in situ* hybridization (FISH), we show colocalization of *Ptn* mRNA with CD13+ pericytes on brain tissue sections (Fig. 4a), with barely detectable and/or very low *Ptn* mRNA expression associated with NeuN+ neurons, GFAP+ astrocytes or Olig2+ oligodendrocytes (Supplementary Fig. 8a–c). Additionally, using FISH we confirmed *Ptn* mRNA expression in pericytes in isolated brain capillaries (Supplementary Fig. 8d), and showed by immunoblotting substantially higher PTN levels in brain pericytes compared to other CNS cell types including brain endothelial cells, oligodendrocyte precursor cells, neurons, VSMCs and astrocytes (Supplementary Fig. 8e). Pericyte ablation resulted in 65% loss of *Ptn+* CD13+ pericytes as shown by FISH (Fig. 4a,b), >60% loss of PTN protein from brain capillaries as shown by immunoblotting (Fig. 4c), and ~65% loss of PTN from CSF at day 9 of DT treatment and 15 days post-DT as shown by sandwich immunoassay (Fig. 4d).

Pericyte-conditioned media containing pericyte-secreted PTN, and mouse recombinant PTN, at concentrations corresponding to physiological CSF PTN levels both protected mouse cortical and hippocampal neurons from cell death induced by withdrawal of neuronal growth medium, oxygen-glucose deprivation and glutamate toxicity (Supplementary Fig. 8f–k), models relevant to brain pathophysiology that develops after pericyte ablation *in vivo* (Supplementary Fig. 5m–o). In all models, the neuroprotective effects of pericyte-conditioned media were abolished by PTN-neutralizing antibody, but not non-immune IgG (Supplementary Fig. 8f–k), consistent with PTN's neuroprotective effects[40–42]. Moreover, restoring PTN loss in pericyte-ablated mice by reinstating physiological CSF PTN levels by a continuous intracerebroventricular infusion of a recombinant mouse PTN from day 6 of DT treatment (when pericyte loss begins) until 15 days post-DT completely prevented neuron loss and behavior deficits, in contrast to control infusion with artificial CSF (Fig. 4e–k).

PTN infusion did not influence, however, cerebrovascular dysfunction in pericyte-ablated mice as indicated by no changes in pericyte loss, CBF loss or BBB breakdown (Supplementary Fig. 9a–l) consistent with data in PTN knockout mice showing no effect on brain vasculature[40]. To determine whether PTN loss alone can trigger neuron loss in mice with intact pericyte coverage and normal circulatory function, we genetically knocked-down *Ptn* by small interfering RNA (si*Ptn*) in TAM-treated pericyte CreER; iDTR mice. Compared to scrambled siRNA, si*Ptn* knockdown depleted *Ptn* from pericytes as shown by FISH (Supplementary Fig. 10a) causing approximately 80% reductions in PTN levels in brain capillaries (Supplementary Fig. 10b) and CSF (Supplementary Fig. 10c). *Ptn* silencing alone, however, did not lead to neuron loss or behavior deficits (Fig. 4f–k) over the same period of time that we show was required for neuron loss to develop after pericyte ablation, and did not affect pericyte coverage (Supplementary Fig. 9a–c) or cerebrovascular integrity (Supplementary Fig. 9g–l). These data suggest that PTN loss is not sufficient to precipitate neuron loss in the absence of circulatory stress that also develops after pericyte loss (Fig. 3a–i). To confirm that circulatory stress is indeed needed to trigger neuron loss in mice with depleted PTN, we challenged si*Ptn*-treated mice with ischemic stroke and excitotoxic lesions. Compared to control siRNA, *Ptn* silencing increased the injury volume and the number of fluoro-jade+ degenerating neurons by 50–60% in both models (Fig. 4l–s), corroborating that PTN loss renders neurons vulnerable to circulatory stress.

DISCUSSION

Our study revealed a rapid neurodegeneration cascade linking pericyte loss to neuron loss by two parallel pathways: i) acute circulatory failure including BBB disruption, development of vasogenic edema, and loss of blood flow; and ii) loss of PTN neurotrophic support (Fig. 4t), which are both required to trigger rapid neuron loss.

In contrast to rapid loss of neurons in pericyte-ablated adult mice, congenital pericyte-deficient mice either do not develop neuron loss, as shown in a model with reduced bioavailability of endothelial platelet-derived growth factor-B (PDGF-BB)[5,43], or develop a late-appearing neuron loss occurring 6–8 months after pericyte loss, as shown in models of globally inherited PDGFRβ deficiency[4,13]. However, PDGFRβ-deficient mice are not

pericyte-specific, and direct loss of PDGFRβ from neural cells[44,45] could also play a role in late neuron loss reported in this model[4]. Fast loss of neurons in pericyte-ablated adult mice, i.e., 20-times faster than in PDGFRβ-deficient mice, is likely related to 60–80 times faster loss of pericytes causing an acute circulatory failure that has not been seen in the previous pericyte-deficient models[4,5,43]. Whether compensatory responses during brain development can influence vascular and/or neuronal phenotype in PDGFRβ-deficient mice, which is not the case in the present ablation model, remains currently unknown and should be addressed by future studies.

Our findings show that pericytes provide a major source of PTN for the brain when compared to other CNS cell types. This is consistent with single cell RNAseq work demonstrating predominant expression of *Ptn* in pericytes compared to low expression in astrocytes, oligodendrocytes and endothelial cells[24], and findings in *Ptn*-EGFP BAC mice (GENSAT project) showing abundant *Ptn* expression in brain vascular profiles consistent morphologically with pericytes, but not in brain parenchymal cells between vascular profiles[39]. In contrast to our present findings and findings by others[5,24,39], another recent single cell transcriptome study using wild type mice suggested that other CNS cell types, as for example arterial endothelial cells express high levels of *Ptn*[46]. When compared with single cell transcriptome studies using endothelial-specific and pericyte-enriched mouse models, one can see that fibroblast markers (e.g., *Igfbp2*, *Pdgfra*, *Lum*, *Dcn*, *Il33*)[24] are associated with the reported "arterial endothelial cells"[46], suggesting a possible contamination of endothelial cells by perivascular fibroblasts - subtype FB1[24]. Using endothelial-specific models[24] previous work did not find *Pdgfra* expression in endothelial cells. Therefore, high *Ptn* expression associated with arterial endothelial cells[46] likely reflects contamination from either physically associated endothelial-fibroblast cell doublets, or fibroblast cell fragments. Compared to brain capillary pericytes, there are only a few FB1 fibroblasts in the CNS localized in penetrating arteries, but not capillaries[24]. Thus, neuronal loss that we see in the hippocampus and cortex after pericyte ablation could not be explained by pericyte-induced loss of PTN in FB1 fibroblasts.

A recent single cell transcriptome study also showed that the highest *Ptn* expression cell type in the CNS are the olfactory glial cells[46]. These cells are found exclusively in the olfactory bulb, not other CNS regions. Therefore, again it is highly unlikely that olfactory unsheathing cells contribute to neuronal injury and loss in the cortex and hippocampus after pericyte ablation in these regions, as we show. Interestingly, a study using wild type mice[46] suggested three subtypes of brain pericytes expressing *Ptn* at levels lower than reported by a previous single cell transcriptome study using pericyte-enriched mouse model indicating single cell type of pericytes in brain[24]. An in-depth look into single cell RNA-seq databases from recent reports using endothelial-specific and/or pericyte-enriched mouse models[24,47], reveals that typical endothelial cell markers such as Claudin 5 (*Cldn5*), *Adgrf5* and *Emcn* are found associated with the suggested pericyte 1 and 2 subtypes[46]. Claudin 5 was shown by many in the field for years including recent reports[24,47], that is a classical endothelial-specific tight junction protein[1]. Additionally, markers suggested to be specific for pericyte 2 subtype (e.g., *Cd82*, *Chst1*, *Apln*)[46] are actually expressed by venous endothelial cells, as reported by a study using endothelial-specific models[24]. Thus, there is a possibility that the reported three pericyte subtypes[46] are actually endothelial-pericyte doublets or pericyte

contaminants with different endothelial fragments, in which case it would be difficult to evaluate cell-specific gene expression in pericytes.

Finally, a study using astrocyte-specific model[48] found high *Ptn* expression in astrocytes that we were not able to show in the present study by either FISH for *Ptn* mRNA and astrocyte marker GFAP (Supplementary Fig. 8b) or by immunoblotting of cultured astrocytes (Supplementary Fig. 8e), similar to findings in a recent single cell transcriptome study[24] and *Ptn*-EGFP BAC mice[39]. The discrepancy between these studies remains unclear, but it might be related to genetic differences between mouse strains such as FVB[48] compared to C57BL/6 in the current and previous[24,39] studies, consistent with strain-specific gene expression in the adult mouse CNS[49].

Acute pericyte loss in the present ablation model mimics well the pathophysiological events seen after ischemic stroke such as development of a rapid BBB breakdown, vasogenic edema and loss of tight junctions. However, after stroke these events result primarily from an acute loss of blood flow, whereas in the present ablation model BBB breakdown after massive loss of pericytes occurs a little before loss of blood flow. The relevance of the present findings to the pathogenesis of chronic neurodegenerative disorders associated with massive regional loss of pericytes and BBB breakdown such as Alzheimer's disease[1,14,17,18], ALS[19], HIV-associated neurocognitive disorder[20], Parkinson's disease and Huntington's disease, is less clear and remains to be determined by future studies. These studies could use preclinical models of these neurological disorders with a different degree of pericyte ablation. Interestingly, recent findings in the living human brain suggested that pericyte degeneration and BBB breakdown are early independent biomarkers of human cognitive dysfunction[50]. Still, whether pericytes die slowly or rapidly in different chronic neurological disorders mandates future studies.

In summary, the present study provides new insights into the pathophysiological mechanisms linking pericyte loss to rapid neuron loss and degeneration. The novel role of pericytes in regulating PTN levels, the consequences for neuroprotection in different pathological scenarios, and how exactly PTN mediates neuroprotection at the molecular level are exciting research directions for future studies. Overall, the present findings could have implications for better understanding the pathogenesis and treatment of acute and chronic CNS disorders associated with pericyte loss and/or neurovascular dysfunction.

Online Methods

Animals

Mice were housed in plastic cages on a 12 h light cycle with ad libitum access to water and a standard laboratory diet. All procedures were approved by the Institutional Animal Care and Use Committee at the University of Southern California with National Institutes of Health guidelines. All animals were included in the study. Animals of both sexes 2–3 months old were used in the experiments. All animals were randomized for their genotype information. All experiments were blinded: the operators responsible for the experimental procedures and data analysis were blinded and unaware of group allocation throughout the experiments. All

mice studied including pericyte-specific Cre mouse line, the Ai14 Cre reporter mice and iDTR mice (see subsections below) were on the same C57Bl/6 background.

Generation of pericyte specific Cre mouse line—A double promoter approach was utilized to achieve pericyte specific expression of Cre recombinase (Fig. 1a). More specifically, we generated two constructs: first, a *Pdgfrβ-Flp construct* that expresses Flippase recombinase (Flp) under the control of the Pdgfrβ promoter[21,51] and second, a *Cspg4-FSF-CreER construct* that carries a *Frt-Stop-Frt-CreER* cassette under the control of Cspg4 promoter[22,52], using a BAC construct carrying the whole mouse *Cspg4* gene and a targeting construct (provided by Dr. Nishiyama at the University of Connecticut) following a standard bacterial recombineering protocol[53]. First, we tested expression of both constructs in cultured primary murine pericytes, brain endothelial cells and vascular smooth muscle cells (VSMCs), and showed that only pericytes co-transfected with *Cspg4-FSF-CreER, Pdgfrβ-Flp* and a GFP reporter, but not endothelial cells or VSMCs, successfully expressed GFP (Fig. S1f,g). The constructs linearized with restriction endonucleases and purified with CsCl gradient method were then co-injected into C57BL/6 blastocysts via pronuclear injection at the Transgenic/Knockout Rodent Core at the University of Southern California. Three litters of 25 pups were born; 5 of them were identified carrying both *Pdgfrβ-flp* cassette and *Cspg4-FSF-CreER* cassette. One founder line (*Pdgfrβ-Flp; Cspg4-FSF-CreER*) was established and verified by PCR and western blotting showing Flippase expression in brain microvessels (Fig. S2a,b), but not capillary-depleted brain. The *Pdgfrβ-Flp; Cspg4-FSF-CreER* line was further characterized by crossing to Ai14 Cre reporter mice which harbor a loxP-flanked STOP cassette preventing transcription of a CAG promoter-driven red fluorescent protein variant (tdTomato; Jackson Laboratory, stock #007908)[29]. Administration of 40 mg/kg per day of Tamoxifen intraperitoneally (i.p.) for seven consecutive days[54] (Sigma #T-5648) released the expression of tdTomato, specifically in pericytes, but not in other brain cell types including endothelial cells, smooth muscle cells, oligodendrocytes, neurons, astrocytes, and microglia (Fig. 1b–e and Fig. S2c–h).

Our initial reasoning of using a double promoter strategy was based on: 1) data showing that PDGFRβ is not expressed in oligodendrocyte precursor cells (OPCs), oligodendrocytes or endothelial cells, as shown by single cell RNAseq analysis[24] and/or immunoblotting of cultured pericytes, VSMCs, OPCs and endothelial cells (Fig. S1a,b); and 2) the quantitative immunoblotting analysis of these cultured cells showing 5–6-fold greater expression of PDGRFβ and NG2 proteins in pericytes compared to VSMCs (Fig. S1a,b), which has been confirmed by immunostaining for both proteins in pericytes and VSMCs on capillaries and arterial retinal vessels, respectively (Fig. S1c,d), as reproted[27]. However, a recent single cell RNAseq study has shown that *Pdgfrb* mRNA is about 4-fold higher in pericytes than in VSMCs, but *Cspg4* mRNA is approximately 1.2-fold higher[24]. Since the steady-state levels of proteins may or may not reflect rates of transcription, it is possible that a fortuitous combination of events led to successful pericyte-specific efficiency. On the other hand, a comparison of subunit stoichiometry and ribosome profiling vs. RNA-seq reads has shown that RNA does not reflect at all subunit stoichiometry, while the translational landscape does[55], which supports our initial idea that the level of proteins mattered in our design.

Nevertheless, the actual data (Fig. 1; Fig. S2) show that the constructs and integration sites used led to a great deal of pericyte-specificity and efficiency.

Diphtheria toxin dependent ablation of pericytes

To generate inducible pericyte ablation model, we crossed our Pericyte-Cre or Pericyte-Cre; Ai14 mice with iDTR mice (Jackson Laboratory #: 007900) for Cre-dependent expression of diphtheria toxin receptor (DTR; from simian Hbegf)[23]. Males and females from both lines were used for breeding and to maintain the colony. Two weeks after the end of Tamoxifen treatment, 2–3 months old Pericyte-Cre; iDTR or Pericyte-Cre; iDTR; Ai14 mice were i.p. administered with 0.1 μg diphtheria toxin (DT, Sigma #D0564) or vehicle per day for 10 consecutive days. Animals were studied at different time points during DT or vehicle treatment and 3 and 15 days post-DT or vehicle injections. 2-month old male and female C3H/HeJ mice (Jackson Laboratory strain # 000659), which are homozygous for retinal degeneration 1 mutation Pde6b[rd1], resulting in retinal degeneration and blindness by weaning age, were used as positive controls for the visual cliff test.

Capillary isolation and capillary-depleted brain collection, and primary cell cultures

Brain capillaries were isolated using dextran gradient centrifugation followed by sequential cell-strainer filtrations, and capillary-depleted brain was also collected, as previously described[56]. The isolated capillaries were collected in PBS and either lysed for immunoblot analysis, cytospun for fluorescent staining analysis, or processed for establishing primary pericyte cell cultures as described below. Capillary-depleted brain samples were lysed for immunoblot analysis.

Brain pericyte culture—Primary mouse brain pericytes were isolated for *in vitro* culturing as we previously described[7,32]. Cultures were confirmed to be morphologically consistent with pericyte cultures and were PDGFRβ-positive, desmin-positive, GFAP-negative, AQP4-negative, MAP2-negative, NeuN-negative, VWF-negative, and Iba1-negative, as we previously reported[32]. Primary mouse pericytes isolated from Cre-inducible DTR transgenic mice (iDTR) mice were transduced with AAV-Cre to render cells sensitive to DT. Pericytes expressing human DTR were then treated with either vehicle, 1×10–4 μg/μL DT or 75 mM potassium chloride (KCl) to measure pericyte contractility and cell death. Pericyte death was assessed utilizing a LIVE/DEAD™ Viability/Cytotoxicity Kit (Thermo Fisher, Cat L3224). Pericyte contractility was assessed by measuring the change in the length of the pericyte along the long axis of the cell, and quantified at 20 minutes, the time point at which the KCl positive control pericytes were fully contracted, and just prior to pericytes beginning to die in DT-treated group. For the duration of the experiments, pericytes were incubated at 37ºC, 21% O_2 and 5% CO_2 in an incubation system for microscopy (KI4, Tokai Hit) and were imaged on a fluorescence microscope (BZ-9000, Keyence). Time-lapse videos were taken immediately upon addition of vehicle, DT or KCl at 3 frames per minute for 45 mins. Pericyte conditioned media for pleiotrophin (PTN) assay and for treating neuronal cultures were collected from 70–80% confluent pericyte cultures 72 h after media change.

Brain endothelial culture—Primary mouse brain endothelial cells were isolated and cultured as previously described[57,58]. Cultures were confirmed to be morphological consistent with primary endothelial cultures with cobble stone-like shape and von Willebrand factor-positive, CD31-positive, VE-cadherin-positive, PDGFRβ-negative, CD13-negative, α-Smooth Muscle Actin (SMA)-negative, NG2-negative, GFAP-negative, AQP4-negative, MAP2-negative, NeuN-negative, and Iba1-negative, as we previously reported[32,58].

Brain VSMCs culture—Primary mouse brain VSMCs were isolated and cultured as previously described[59,60]. Cultures were confirmed to be morphologically consistent with VSMC cultures and were SMA-positive, calponin-positive, SM22α-positive, von Willebrand factor-negative, GFAP-negative, AQP4-negative, MAP2-negative, NeuN-negative, Iba1-negative, and prolyl-4-hydroxylase-negative, as we previously reported[59].

Mouse oligodendrocyte culture—A2B5-positive oligodendrocyte precursor cells (OPCs) were isolated from cortices of P5 mouse pups by magnetic cell sorting (MACS, Miltenyi Biotec), as we previously described[8].

Neuronal Cultures—Neuronal cells were isolated from the cortex and hippocampus of E14.5 mouse embryos as we previously described[61].

i) B27 withdrawal: Primary mouse cortical neurons were cultured for 10 days with B27 supplement followed by B27 withdrawal for 48 hrs. Pericyte conditioned media diluted to contain pericyte-secreted PTN levels at a concentration to match mouse *in vivo* PTN CSF concentration (~3 nM) with and without PTN neutralizing antibody (Anti-PTN, R&D systems, AF-252; 500 ng/ml) or non-immune IgG (NI IgG; Santa Cruz, sc-2027; 500ng/ml), or mouse recombinant PTN (3.5 nM; R&D systems, 6580-PL), were added to media to assess neuronal survival.

ii) Oxygen and glucose deprivation (OGD) and glutamate treatment: OGD and glutamate treatment were performed using 10 days old neuronal cultures. For OGD, neuronal media was replaced with glucose-free DMEM (Invitrogen) supplemented with pericyte conditioned media with and without PTN neutralizing antibody, NI IgG, and mouse recombinant PTN as above in i), and then transferred in a humidified incubator chamber (Billups-Rothenberg, Inc.) with 1% O_2 at 37°C for 3 h. After 3 h, cells were removed from the chamber and processed for immunocytochemistry 24h later. For glutamate treatment, 10 μM glutamate were added to neuronal media as previously described[41], and pericyte conditioned media, PTN neutralizing antibody, NI IgG, and PTN were added as above in i).

Astrocytes—Cortical astrocytes were isolated and cultured from P1 to P4 pups from B6 mice as previously described[62].

Immunohistochemistry

Animals were anesthetized, perfused and brains were removed and postfixed as we previously described[8]. Kidney, liver, heart and skeletal muscle tissue were also collected, postfixed and cut at 30 μm thickness using a vibratome (Leica). Retinas were processed as previously described[63]. Brain sections were cut at 30 μm thickness and were blocked with

5% normal donkey serum (Vector Laboratories)/0.1%Triton-X/0.01M PBS and incubated with primary antibodies diluted in blocking solution overnight at 4°C. All antibodies are listed in Supplementary Table 1. To visualize brain microvessels, sections were incubated with Dylight 488, 594 or 647-conjugated L. esculentum Lectin as we have previously reported[4,58]. After incubation with primary antibodies, sections were washed in PBS and incubated with fluorophore-conjugated secondary antibodies (see Supplementary Table 1) and then mounted onto slides with DAPI (4',6-diamidino-2-phenylindole) fluorescence mounting medium (Dako). Sections were imaged with a Zeiss LSM 510 confocal laser-scanning microscope as we previously described[8]. Z-stack projections and pseudo-coloring were performed using ZEN software (Carl Zeiss Microimaging). Image post-analysis was performed using ImageJ software. See Supplementary Table 1 for antibody details and dilutions used.

In situ fluorescent TUNEL staining—Tissue was incubated for 30 min in 20 μg/ml Proteinase K and the In Situ Cell Death Detection Kit (Roche) was used per the manufacturer's instructions. Sections were coverslipped as described above. For quantification, TUNEL-positive cells that also demonstrated tdTomato-positive pericyte expression were quantified by using the ImageJ Cell Counter analysis tool. In each animal, 5 randomly selected fields from the cortex were analyzed in 3 non-adjacent sections (~100 μm apart). Three animals per group were analyzed.

Quantification

For *Pericyte coverage and numbers, Extravascular leakages, NeuN-Positive Neuronal Nuclei Counting, MAP2+ neuron counts, Neurofilament (SMI-312)-Positive Axons, Oligodendrocyte counts, Microglial Quantification, and GFAP-Positive Astrocyte Counting, and aquaporin 4 coverage,* for each animal, 4–6 randomly selected fields in the somatosensory cortex region and/or the CA1 region of the hippocampus were analyzed in 3–4 non-adjacent sections (~100 μm apart), and averaged per mouse.

Pericyte coverage and numbers—For pericyte coverage and cell numbers, ten-micron maximum projection z-stacks (area 640×480 μm) were reconstructed, and the areas occupied by CD13-positive (pericyte) and lectin-positive (endothelium) fluorescent signals or CD13-positive perivascular cell bodies that co-localized with DAPI-positive nuclei on the abluminal side of lectin-positive endothelium on vessels < 6 μm were analyzed using ImageJ as we previously described[64]. Five animals per group were analyzed.

Smooth muscle cell wall thickness and number analysis—For analysis of the VSMCs-covered arteriolar vessel wall thickness, we studied penetrating arterioles (> 25 μm in diameter) from the cortical layer 1 in the somatosensory cortex region. 200 μm SMA-positive segments were selected randomly for diameter measurements from maximum intensity projections of 30 μm optical stacks, as we previously reported[64].

NeuN-Positive Neuronal Nuclei Counting—NeuN-positive neurons were quantified using the ImageJ Cell Counter analysis tool. Five animals per group were analyzed.

MAP2+ neuron counts—For quantification of primary cortical and hippocampal cultured neuron numbers, four fields per coverslip from three coverslips were randomly chosen using a 20x objective on a BZ-900 fluorescent microscope. The total number of MAP2+DAPI+ neurons was divided by the total number of DAPI+ cells measured using ImageJ Cell Counter plugin. Data is expressed as the percentage of (MAP2+ DAPI+ neurons/ DAPI+ cells) X 100, as previously reported[65,66].

Neurofilament (SMI-312)-Positive Axons—As we previously described[4,8], ten micron maximum projection z-stacks were reconstructed, and SMI-312-positive signal was subjected to threshold processing and analysis using ImageJ. Five animals per group were analyzed.

Microglial Quantification—The number of Iba1-positive microglia that also demonstrated DAPI- positive nuclear staining was quantified using the ImageJ Cell Counter analysis tool. Three animals per group were analyzed.

GFAP-Positive Astrocyte Counting—The number of GFAP-positive astrocytes that also demonstrated DAPI- positive nuclear staining were quantified by using the ImageJ Cell Counter analysis tool. Three animals per group were analyzed.

Aquaporin 4 coverage—Ten-micron maximum projection z-stacks (area 640×480 um) were reconstructed and Aquaporin 4 expression around microvessels was quantified by calculating the area occupied by Aquaporin 4 versus lectin area using ImageJ. Three animals per group were analyzed.

Oligodendrocyte Counts—Ten microns maximum projection z-stacks were reconstructed, and the number of Olig2-positive oligodendrocytes per mm2 were determined using the ImageJ Software Cell Counter plugin analysis tool. Three animals per group were analyzed.

Immunofluorescent ZO-1 and occludin tight junction and VE-Cadherin adherens junction analysis—The length of ZO-1, occludin, and VE-Cadherin-positive signals on lectin-positive capillary profiles in the cortex and the hippocampus was determined as we have previously reported[32]. The length of ZO1, occludin, and VE-Cadherin-positive tight and adherens junction proteins was normalized to the total area of lectin-positive microvessels using the ImageJ Area measurement tool. Five animals per group were analyzed.

Extravascular leakages—Perivascular blood-derived fibrin(ogen) and IgG deposits indicating blood-brain barrier (BBB) breakdown were measured as we previously described[4,7,32,67]. For quantification of extravascular fibrin(ogen) deposits, an antibody that detects both fibrinogen and fibrinogen-derived fibrin polymers was used. Ten-micron maximum projection z-stacks were reconstructed, and the fibrin(ogen)-positive perivascular signal on the abluminal side of lectin-positive endothelial profiles on microvessels < 6 μm in diameter was analyzed using ImageJ[4,64]. Five animals per group were analyzed.

Western blots

Capillaries and capillary-depleted brains were lysed in RIPA buffer (50 mM Tris, pH 8.0, 150 mM NaCl, 0.1% SDS, 1.0% NP-40, 0.5% sodium deoxycholate and Roche protease inhibitor cocktail), subjected to SDS-Page gel electrophoresis and transferred to a nitrocellulose membrane. Membranes were blocked with 5% milk, incubated with primary antibody, and then incubated with the appropriate HRP-conjugated secondary antibody. Membranes were then treated with Immobilon Western ECL detection buffers (Millipore), exposed to CL-XPosure film (Thermo Scientific) and developed in a X-OMAT 3000 RA film processor (Kodak). Primary antibodies used for western blotting were rabbit monoclonal anti-mouse PDGFRβ (Cell Signaling, 3169S, 1:000), goat polyclonal anti-mouse CD31 (R&D Systems, AF3628, 1:1000), mouse monoclonal anti-human DTR (BioAcademia, 71–501, 1:1000), rabbit monoclonal anti-mouse VE-Cadherin (Abcam, ab205336, 1:1000), rabbit anti-ZO-1 antibody (Invitrogen, 40–2200, 1:1000), mouse anti-occludin antibody (BD Biosciences, 611091, 1:500), Rabbit anti-Claudin 5 (Abcam, ab15106, 1:1000), Rabbit anti-PTN (Sino Biological Inc, 51000-T40, 1:1000), Rabbit polyclonal Flp recombinase antibodies, (OriGene, TA160030, 1:500), Rabbit anti-GAPDH (Cell Signaling Technology, 5174S, 1:1000), rabbit polyclonal anti-mouse β-actin (Cell Signaling, 4970S, 1:1000), HRP-conjugated horse anti-mouse secondary antibody (Cell Signaling, 7076S, 1:5000) and HRP-conjugated donkey anti-rabbit secondary antibody (Invitrogen, A16023, 1:5000).

Laser-Doppler flowmetry CBF measurement

CBF response to 400 μm adenosine applied through an open cranial window was measured using laser-Doppler flowmetry (LDF) in mice under 1% isoflurane anesthetic as described[13,68,69]. The percentage increase in CBF due to adenosine application was obtained by subtracting the baseline CBF from the maximum value reached within 5 min of drug application, divided by the basal CBF value.

Magnetic Resonance Imaging (MRI)

All MRI scans were performed using our MR Solutions 7T PET-MR system (bore size ~24-mm, up to 600 mT.m^{-1} maximum gradient (MR Solutions Ltd., Guildford, UK) and a 20-mm internal diameter quadrature bird cage mouse head coil.

Mice were anesthetized by 1–1.2% isoflurane in air. Respiration rate (72.0 ± 5.0 breaths per minute) and body temperature (36.5 ± 0.5°C) were monitored during the experiments as we previously described[8]. The sequences were collected in the following order: T2-weighted (2D-fast spin echo (FSE), TR/TE 4,000/26 ms, 32 slices, slice thickness 300 μm, in-plane resolution 100×70 μm^2) to obtain structural images; diffusion weighted echo-planar imaging (EPI, TR/TE 5,000/32, 14 slices, 1 b-value, 7 directions, slice thickness 300 μm, in-plane resolution 200×300 μm^2) to assess brain edema; dynamic contrast-enhanced (DCE) protocol for the capillary permeability assessment; and finally, dynamic susceptibility-contrast (DSC) imaging for regional cerebral blood flow. Total imaging time was approximately 40 min per mouse.

The DCE-MRI imaging protocol was performed within the dorsal hippocampus territory, and included measurement of pre-contrast T1-values using a variable flip angle (VFA) fast low angle shot (FLASH) sequence (FA = 5, 10, 15, 30 and 45°, TE = 3 ms, slice thickness 1 mm, in-plane resolution 60×120 μm^2), followed by a dynamic series of 180 T1-weighted images with identical geometry and a temporal resolution of 5.1 s (FLASH, TR/TE = 20/3 ms, flip angle 15°, slice thickness 1 mm, in-plane resolution 60×120 μm^2). Using a power injector, a bolus dose (140 μL) of 0.5 mmol/kg Gd-DTPA (Gadolinium-diethylenetriamine pentaacetic acid, Magnevist®, diluted in saline 1:4) was injected via the tail vein at a rate of 600 μL/min. DCE images were collected over 10 min after the injection. The DSC-MRI imaging was performed on the exact same geometry. A dynamic series of 80 T2*-weighted images is used, with a temporal resolution of 1.4 s (FLASH, TR/TE = 18/3 ms, slice thickness 1 mm, flip angle 15°, in-plane resolution 120×230 μm^2). A second bolus dose of either (140 μL) of Gd-DTPA (1:1 dilution) or Ferimoxytol (Ferahene®, 1:2 dilution) was injected via the tail vein at a rate of 1000 μL/min. DSC images were collected over 85 s after the injection.

MRI Post-Processing Analysis

Capillary Permeability Assessment

<u>**T1 Mapping:**</u> T1 relaxation times were estimated using the VFA method, prior to Gd-DTPA injection, with a series of FLASH images with varying FA and constant TR and TE using the standard saturation recovery equation:

$$SI = SI_{(TR \gg T1, TE \ll T2*, \theta = 90°)} \frac{\sin(\theta - E_1)E_2}{1 - E_{1cos\theta}}$$

Where SI is the signal intensity and where θ is the FA, $E_1 = e^{-TR/T1}$ and $E_2 = e^{-TE/T2*}$. Here, we assume that TE < T2*. Non-linear least-squares fitting is used to fit MRI data to the equation above.

<u>**K_{trans} Mapping:**</u> Post-processing of the collected DCE-MRI data was performed using in-house DCE processing software (*Rocketship*) implemented in Matlab[70]. The unidirectional capillary transfer constant, K_{trans}, to intravenously injected gadolinium-based contrast agent was determined in both primary somatosensory cortex and hippocampus in mice using a modified method as we reported in humans[71] with the post-processing Patlak analysis[8,70,72]. We determined the arterial input function (AIF) in each mouse from the common carotid artery, as previously reported[8,71].

Cerebral Blood Flow Assessment—Following collection of the DSC-MRI data, quantitative post-processing analysis was optimized as we and others previously reported[8,73].

Brain Edema Assessment—Diffusion tensor imaging (DTI)-EPI parametric maps were generated using DSI Studio (March 6, 2018 build; dsi-studio.labsolver.org) as previously described[74]. The diffusion weighted image data was pre-processed with motion, ghosting

and eddy current corrections. After the co-registration of all individual images, data means were extracted for ADC (apparent diffusion coefficient; $x10^{-3}$ mm^2/s) through DSI studio using the following equation:

$$ADC = -b\ln(\frac{S}{S_0})$$

Where S_0 is the signal intensity without the diffusion weighting, S is the signal with the diffusion gradient and *b* is the b-value. ROIs for primary somatosensory cortex and dorsal hippocampus were manually assigned by an investigator blinded to groups. To examine distinct changes, regional ROIs were drawn on ADC maps using boundaries defined by the Allen brain atlas (http://mouse.brain-map.org/).

Behavioral tests

Novel object location—Novel object location test was performed as we previously reported[4,7]. Four time points were analyzed in TAM-treated Pericyte-CreER; iDTR mice; before DT (n=7) or vehicle (n=8) treatment, 6 days after DT (n=9) or vehicle (n=6) treatment, 3 days post-DT (n=7) or vehicle (n=11) treatment, and 15 days post-DT (n=7) or vehicle (n=14) treatment, 15 days post-DT treatment with PTN (n=5) or aCSF (n=7) ICV infusion, or two weeks after si*Ptn* (n=6) or siControl (n=7) injections.

Contextual fear conditioning—Long-term memory formation paradigm in contextual fear conditioning was adapted from a previously described protocol[75]. During training, mice were placed in the conditioning chamber for 5 minutes and received four footshocks (0.25 mA, 1 sec) at 1-minute interval starting 2 minutes after placing the mouse in the chamber. Contextual long-term memory was tested in the same chamber the next day without footshock applied. The experiment was performed in TAM-treated Pericyte-CreER; iDTR mice 3 days post-DT (n=10) or vehicle (n=10) treatment, 15 days post-DT (n=6) or vehicle (n=9) treatment, 15 days post-DT treatment with PTN (n=5) or aCSF (n=7) ICV infusion, or two weeks after si*Ptn* (n=5) or control siRNA (n=7) injections.

Visual cliff test—Test was performed as previously described[76,77] with modifications. A transparent Plexiglas square arena (30 × 30 cm) was divided into two equal parts by aligning the middle of the arena with the edge of the table. The side sitting on the tabletop was considered a "shallow" side and the other one that is positioned over the floor area (50 cm high) a "deep" side. A 3 cm black and white checked paper floor was placed bellow the arenas: immediately below the Plexiglas surface on the shallow side, and on the floor on the deep side creating an illusion of a cliff. The animal's behavior was recorded using Noldus Ethovision software with a camera placed above the arena. Each animal was placed on the shallow side and the total time spent exploring each side of the arena was recorded within a 5 min trial. The percentage time spent in the shallow side was analyzed.

In vivo two-photon laser scanning microscopy (TPLSM) of red blood cell (RBC) velocity and capillary diameter

Animals were initially anesthetized with 100 mg/kg of ketamine and 10 mg/kg of xylazine and were placed on a heating pad (37°C). A 5 mm diameter cranial window was implanted over the somatosensory cortex as previously described[78]. Animals were allowed to rest for 3 hours before imaging. RBC velocity through individual capillaries in the top 200 μm (layers I-II) of somatosensory cortex in mice under 0.5% isoflurane was determined using vessel linescans (113 lines/s, 120 nm/pixel) of RBC passage as detailed previously[13,78] under resting conditions after retro-orbital injection with 70 kDa Texas Red (TxRed)-labeled dextran. Capillary segments were randomly chosen for diameter cross-section measurement using ImageJ from high resolution (120 nm/pixel) average intensity projections of 60 μm optical substacks through the same tissue volume as the velocity measurements. Cross-sections were analyzed for diameter in Igor Pro (WaveMetrics). Two measurements per vessel segment were averaged per vessel.

Hypoxia

For determination of hypoxic tissue mice were injected intraperitoneally with 60 mg/kg hypoxyprobe-1 pimonidazole (Hypoxyprobe-1™ Plus Kit) as we previously described[4,8].

Fluorescence in situ hybridization (FISH)

RNA FISH was performed using the RNAscope technology (Advanced Cell Diagnostics). Tissue sample preparation and pretreatment was performed on both fresh frozen isolated microvessels cytospun onto glass slides (Catalog no. 320513) and fixed brains cut into 20-μm coronal sections mounted onto SuperFrost Plus glass slides (Catalog no. 320535) following the manufacturer's protocols. After dehydration and pretreatment, slides were subjected to RNAscope Multiplex Fluorescent Assay (Catalog no. 320293). RNAscope probes for mouse-*Ptn*, positive control and negative control were hybridized for 2 h at 40°C in the HybEZ Oven and the remainder of the assay protocol was implemented. Subsequently, the slides were subjected to immunohistochemistry (see immunohistochemistry Methods section). The fluorescent signal emanating from RNA probes and antibodies was visualized and captured using a Nikon A1R MP+ confocal/multiphoton microscope (Nikon). All FISH images presented are projections of ~6-μm z-stacks (0.3 μm interval) obtained from cerebral cortex, and a smoothing algorithm was applied during image post-processing (Nikon NIS-Elements Software).

Cerebrospinal fluid extraction (CSF) and glutamate measurements

CSF was extracted as we previously described[71,79]. Glutamate was measured using Glutamate Assay Kit (Sigma, MAK004) per manufacturer's instructions.

PTN assay

PTN levels in mouse CSF and pericyte conditioned medium were measured by a sandwich immunoassay using the Meso Scale Discovery (MSD) platform. First, standard-bind 96-well plates (MSD, L15XA-3) were coated with a capture antibody (Sino Biological Inc, 51000-T40) per manufacturer's instructions. After sample incubation, the plate was washed and the

incubated for 1 hour with human PTN biotinylated antibody which cross-reacts with mouse PTN (R&D systems BAF252) and 1 μg/mL of Sulfo-tag labeled streptavidin (MSD). The plate was read immediately on the MSD SECTOR Imager 6000. PTN concentration in samples were calculated based on a recombinant mouse PTN (R&D systems, 6580-PL) standard curve.

Intracerebral osmotic pump implantation and infusion

To infuse mouse PTN into the brain, we used an MRI-compatible intracerebral infusion system that consists of a modified intracerebral 3 mm fused silica cannula with plastic hub (Alzet Brain Infusion Kit 3, DURECT Corp., Cupertino, CA; custom modified by Plastics One, Roanoke, VA, product #3280PM-PK-SPC), which is connected to a small capsule-shaped osmotic pump (200 μl capacity; 3.0 cm length × 0.7 cm diameter; Alzet model 2004, DURECT Corp.) with peek micro medical tubing (DURECT Corp., Cupertino, CA, product #0002612) that continuously infused PTN at 0.11 μl per hour for up to four weeks. After filling up each pump and connected tubing with mouse recombinant PTN (R&D systems, 6580-PL; 15 μg/ml) dissolved in artificial CSF (aCSF) or aCSF only, the osmotic pumps were surgically implanted subcutaneously in the flanks of sedated mice and secured with skin sutures on day 6 of DT injections. The intracerebral cannula was stereotaxically implanted bilaterally in both lateral ventricles at the location 0.3 mm caudal to the Bregma, 1.3 mm lateral of midline, and 3 mm below the surface of the brain, and the hub was anchored to the cranial surface with cyanoacrylate adhesive. Surgical wounds were closed with cyanoacrylate adhesive and sutures over the hub. Mice were observed under radiant and blanket warmers until recovered from sedation and monitored for ill effects. On a technical note, the PTN CSF measurements after infusion with aCSF and PTN (15 μg/ml) indicated mean + s.e.m. PTN CSF levels of 0.93 + 0.04 nM (n=3) and 3.19 + 0.39 nM (n=4), respectively, confirming that aCSF-infused mice had levels comparable to those found in TAM-treated CreER; iDTR mice after pericyte ablation, whereas PTN-infused mice showed levels comparable to those found in control TAM-treated CreER; iDTR treated with vehicle, respectively (see Fig. 4d). Of note, mouse CSF production is estimated to be 18 μl per hour, or ~ 165 times faster than the presently used ICV infusion rate (i.e., 0.11 μl per hour) suggesting that ICV infusion has minimal dilution effect. These results show that PTN infusion was able to increase PTN CSF levels and delivery of PTN to CNS after pericyte ablation to levels comparable to those found in control mice.

siRNA Gene Silencing

To knockdown *Ptn* in Pericyte-Cre mice, we used *Ptn*-specific chemically modified, 21-mer, double-stranded Ambion® In Vivo siRNA (ThermoFisher), following our previously described approach[8]. As *Ptn* in mice is only expressed in the brain and not in peripheral tissues, as shown by the mouse genome project[38], and is enriched in pericytes, as we (Fig. 4a–c; Fig S8d,e) and others[5,24,39] show, to short term silence *Ptn* we administered centrally si*Ptn* or scrambled control siRNA by bilateral intracerebroventricular injection.

Transient middle cerebral artery occlusion (MCAo)

Transient MCAo was performed as previously described with modifications[80]. For stroke studies 2 weeks after si*Ptn* or control siRNA ICV injections we used 30 minute MCAo and

24 hr reperfusion (Fig. 4l,m); for leucocyte and platelet control immunostaining we used 3 h MCAo and 24 h reperfusion (Fig. S5c); for edema (ADC) values after stroke we used 1 h MCAo and 15 days reperfusion (Fig. S5g). Infarction volume was determined as previously described[80]. Fluoro-Jade B staining (EMD Millipore, AG310) was performed per manufacturer's instructions.

NMDA treatment

Animals received NMDA injections in the right striatum (0.5 mm anterior, 2.0 mm lateral, 3.5 mm ventral) at a concentration of 20 nmol in 0.3 μLof PBS, as we previously described[81] two weeks after si*Ptn* or control siRNA. Two days later the animals were sacrificed and tissue was processed as described above.

Electron Microscopy (EM)

Anesthetized vehicle and DT-treated animals were injected retro-orbitally with horseradish peroxidase Type II (HRP ii; MW=44 kDa) at a dosage of 10 mg/20g of body weight (Sigma, P8250) and were sacrificed 2 hours later. Animals were perfused and brains were removed and cut as we previously described[8]. HRP-diaminobenzidine (DAB) cytochemistry was performed on brain sections per manufacturer's instructions (Sigma, D3939). Sections were then processed as previously described[8]. Parts of the cortex were carefully dissected and placed on Epon blocks under a stereoscope. Blocks were coded, and all subsequent procedures were performed blind to genotypes. Seventy-nanometer thin sections were obtained on copper mesh grids using a Reichert ultramicrotome with a diamond knife (Diatome, Biel, Switzerland) and ultrastructural analysis was performed using a JEOL JEM-2100 transmission electron microscope as we previously described[8].

Analysis of Systemic Parameters

Heart rate were monitored by electrocardiography. For respiration rate, an MRI pressure pad/respiration transducer was used (TSD110, Biopac Systems, Goleta, CA), where the anesthetized animal was placed on top of the pad to record respiration. The pH, glucose levels, and blood gases were determined from a small sample (~90 μL) of arterial blood, collected from the cannulated right femoral artery, using the i-STAT CG8+ panel (03P88–25, Abbott, Princeton, NJ). For analysis of liver and kidney function ~500 μl of serum was collected from the heart and sent to Idexx Reference Laboratories (North Grafton, MA) for screening (test codes 60405 and 60406, respectively).

Quantification and statistical analysis

Sample sizes were calculated using nQUERY assuming a two-sided alpha-level of 0.05, 80% power, and homogeneous variances for the 2 samples to be compared, with the means and common standard deviation for different parameters predicted from published data and our previous studies[4,7,8,13,32]. Data are presented as mean ± s.d. or mean ± s.e.m. as indicated in the figure legends. For parametric comparison between two groups, F test was conducted to determine the similarity in the variances between the groups that are statistically compared, and statistical significance was analyzed by Student's t-test. For multiple comparisons, Bartlett's test for equal variances was used to determine the variances

between the multiple groups and one-way analysis of variance (ANOVA) followed by Bonferroni's post hoc test was used to test statistical significance, using GraphPad Prism software. Data was tested for normality using the Shapiro-Wilk test. A P-value of less than 0.05 was considered statistically significant.

Code availability

We used our graphical user interface (GUI) code (https://github.com/petmri/ROCKETSHIP) running with MATLAB R2019a version (and anterior versions) for DCE-MRI and DSC-MRI analyses.

Life Sciences Reporting Summary

Additional information regarding methodology, statistics, software, study design, and antibody validation is included in the accompanying Life Sciences Reporting Summary.

Data Availability

The data that support the findings of this study are available from the corresponding author upon request.

Supplementary Material

Refer to Web version on PubMed Central for supplementary material.

Acknowledgments

References

1. Sweeney MD, Zhao Z, Montagne A, Nelson AR & Zlokovic BV Blood-Brain Barrier: From Physiology to Disease and Back. Physiol. Rev 99, 21–78 (2019). [PubMed: 30280653]

2. Sweeney MD, Ayyadurai S & Zlokovic BV Pericytes of the neurovascular unit: key functions and signaling pathways. Nat. Neurosci 19, 771–783 (2016). [PubMed: 27227366]

3. Gaengel K, Genové G, Armulik A & Betsholtz C Endothelial-mural cell signaling in vascular development and angiogenesis. Arterioscler. Thromb. Vasc. Biol 29, 630–638 (2009). [PubMed: 19164813]

4. Bell RD et al. Pericytes control key neurovascular functions and neuronal phenotype in the adult brain and during brain aging. Neuron 68, 409–427 (2010). [PubMed: 21040844]

5. Armulik A et al. Pericytes regulate the blood-brain barrier. Nature 468, 557–561 (2010). [PubMed: 20944627]

6. Daneman R, Zhou L, Kebede AA & Barres BA Pericytes are required for blood-brain barrier integrity during embryogenesis. Nature 468, 562–566 (2010). [PubMed: 20944625]

7. Sagare AP et al. Pericyte loss influences Alzheimer-like neurodegeneration in mice. Nat. Commun 4, 2932 (2013). [PubMed: 24336108]

8. Montagne A et al. Pericyte degeneration causes white matter dysfunction in the mouse central nervous system. Nat. Med 24, 326–337 (2018). [PubMed: 29400711]

9. Ma Q et al. Blood-brain barrier-associated pericytes internalize and clear aggregated amyloid-β42 by LRP1-dependent apolipoprotein E isoform-specific mechanism. Mol. Neurodegener 13, 57 (2018). [PubMed: 30340601]

10. Peppiatt CM, Howarth C, Mobbs P & Attwell D Bidirectional control of CNS capillary diameter by pericytes. Nature 443, 700–704 (2006). [PubMed: 17036005]

11. Hall CN et al. Capillary pericytes regulate cerebral blood flow in health and disease. Nature 508, 55–60 (2014). [PubMed: 24670647]

12. Mishra A et al. Astrocytes mediate neurovascular signaling to capillary pericytes but not to arterioles. Nat. Neurosci 19, 1619–1627 (2016). [PubMed: 27775719]

13. Kisler K et al. Pericyte degeneration leads to neurovascular uncoupling and limits oxygen supply to brain. Nat. Neurosci 20, 406–416 (2017). [PubMed: 28135240]

14. Sweeney MD, Sagare AP & Zlokovic BV Blood-brain barrier breakdown in Alzheimer disease and other neurodegenerative disorders. Nat. Rev. Neurol 14, 133–150 (2018). [PubMed: 29377008]

15. Zehendner CM et al. Traumatic brain injury results in rapid pericyte loss followed by reactive pericytosis in the cerebral cortex. Sci. Rep 5, 13497 (2015). [PubMed: 26333872]

16. Ghosh M et al. Pericytes are involved in the pathogenesis of cerebral autosomal dominant arteriopathy with subcortical infarcts and leukoencephalopathy. Ann. Neurol 78, 887–900 (2015). [PubMed: 26312599]

17. Sengillo JD et al. Deficiency in mural vascular cells coincides with blood-brain barrier disruption in Alzheimer's disease. Brain Pathol. Zurich Switz 23, 303–310 (2013).

18. Halliday MR et al. Accelerated pericyte degeneration and blood-brain barrier breakdown in apolipoprotein E4 carriers with Alzheimer's disease. J. Cereb. Blood Flow Metab. Off. J. Int. Soc. Cereb. Blood Flow Metab 36, 216–227 (2016).

19. Winkler EA et al. Blood-spinal cord barrier breakdown and pericyte reductions in amyotrophic lateral sclerosis. Acta Neuropathol. (Berl.) 125, 111–120 (2013). [PubMed: 22941226]

20. Niu F, Yao H, Zhang W, Sutliff RL & Buch S Tat 101-mediated enhancement of brain pericyte migration involves platelet-derived growth factor subunit B homodimer: implications for human immunodeficiency virus-associated neurocognitive disorders. J. Neurosci. Off. J. Soc. Neurosci 34, 11812–11825 (2014).

21. Cuttler AS et al. Characterization of Pdgfrb-Cre transgenic mice reveals reduction of ROSA26 reporter activity in remodeling arteries. genesis 49, 673–680 (2011). [PubMed: 21557454]

22. Zhu X et al. Age-dependent fate and lineage restriction of single NG2 cells. Dev. Camb. Engl 138, 745–753 (2011).

23. Buch T et al. A Cre-inducible diphtheria toxin receptor mediates cell lineage ablation after toxin administration. Nat. Methods 2, 419–426 (2005). [PubMed: 15908920]

24. Vanlandewijck M et al. A molecular atlas of cell types and zonation in the brain vasculature. Nature 554, 475–480 (2018). [PubMed: 29443965]

25. Sagare AP, Sweeney MD, Makshanoff J & Zlokovic BV Shedding of soluble platelet-derived growth factor receptor-β from human brain pericytes. Neurosci. Lett 607, 97–101 (2015). [PubMed: 26407747]

26. Zeisel A et al. Brain structure. Cell types in the mouse cortex and hippocampus revealed by single-cell RNA-seq. Science 347, 1138–1142 (2015). [PubMed: 25700174]

27. Trost A et al. Brain and Retinal Pericytes: Origin, Function and Role. Front. Cell. Neurosci 10, 20 (2016). [PubMed: 26869887]

28. Feil R, Wagner J, Metzger D & Chambon P Regulation of Cre recombinase activity by mutated estrogen receptor ligand-binding domains. Biochem. Biophys. Res. Commun 237, 752–757 (1997). [PubMed: 9299439]

29. Madisen L et al. A robust and high-throughput Cre reporting and characterization system for the whole mouse brain. Nat. Neurosci 13, 133–140 (2010). [PubMed: 20023653]

30. Yamaizumi M, Mekada E, Uchida T & Okada Y One molecule of diphtheria toxin fragment A introduced into a cell can kill the cell. Cell 15, 245–250 (1978). [PubMed: 699044]

31. Parkhurst CN et al. Microglia promote learning-dependent synapse formation through brain-derived neurotrophic factor. Cell 155, 1596–1609 (2013). [PubMed: 24360280]

32. Bell RD et al. Apolipoprotein E controls cerebrovascular integrity via cyclophilin A. Nature 485, 512–516 (2012). [PubMed: 22622580]

33. Berthiaume A-A et al. Dynamic Remodeling of Pericytes In Vivo Maintains Capillary Coverage in the Adult Mouse Brain. Cell Rep. 22, 8–16 (2018). [PubMed: 29298435]

34. Park DY et al. Plastic roles of pericytes in the blood-retinal barrier. Nat. Commun 8, 15296 (2017). [PubMed: 28508859]

35. Ogura S et al. Sustained inflammation after pericyte depletion induces irreversible blood-retina barrier breakdown. JCI Insight 2, e90905 (2017). [PubMed: 28194443]

36. Lin S-L, Kisseleva T, Brenner DA & Duffield JS Pericytes and perivascular fibroblasts are the primary source of collagen-producing cells in obstructive fibrosis of the kidney. Am. J. Pathol 173, 1617–1627 (2008). [PubMed: 19008372]

37. Stefanska A et al. Interstitial pericytes decrease in aged mouse kidneys. Aging 7, 370–382 (2015). [PubMed: 26081073]

38. Yue F et al. A comparative encyclopedia of DNA elements in the mouse genome. Nature 515, 355–364 (2014). [PubMed: 25409824]

39. Gong S et al. A gene expression atlas of the central nervous system based on bacterial artificial chromosomes. Nature 425, 917–925 (2003). [PubMed: 14586460]

40. Krellman JW, Ruiz HH, Marciano VA, Mondrow B & Croll SD Behavioral and neuroanatomical abnormalities in pleiotrophin knockout mice. PloS One 9, e100597 (2014). [PubMed: 25000129]

41. Asai H, Morita S & Miyata S Effect of pleiotrophin on glutamate-induced neurotoxicity in cultured hippocampal neurons. Cell Biochem. Funct 29, 660–665 (2011). [PubMed: 21928404]

42. Dugas JC et al. A novel purification method for CNS projection neurons leads to the identification of brain vascular cells as a source of trophic support for corticospinal motor neurons. J. Neurosci. Off. J. Soc. Neurosci 28, 8294–8305 (2008).

43. Keller A et al. Mutations in the gene encoding PDGF-B cause brain calcifications in humans and mice. Nat. Genet. 45, 1077–1082 (2013). [PubMed: 23913003]

44. Ishii Y et al. Mouse brains deficient in neuronal PDGF receptor-beta develop normally but are vulnerable to injury. J. Neurochem 98, 588–600 (2006). [PubMed: 16805849]

45. Zheng L et al. Neuroprotective effects of PDGF against oxidative stress and the signaling pathway involved. J. Neurosci. Res 88, 1273–1284 (2010). [PubMed: 19998489]

46. Zeisel A et al. Molecular Architecture of the Mouse Nervous System. Cell 174, 999–1014.e22 (2018). [PubMed: 30096314]

47. Sabbagh MF et al. Transcriptional and epigenomic landscapes of CNS and non-CNS vascular endothelial cells. eLife 7, (2018).

48. Zhang Y et al. An RNA-sequencing transcriptome and splicing database of glia, neurons, and vascular cells of the cerebral cortex. J. Neurosci. Off. J. Soc. Neurosci 34, 11929–11947 (2014).

49. Sandberg R et al. Regional and strain-specific gene expression mapping in the adult mouse brain. Proc. Natl. Acad. Sci. U. S. A 97, 11038–11043 (2000). [PubMed: 11005875]

50. Nation DA et al. Blood-brain barrier breakdown is an early biomarker of human cognitive dysfunction. Nat. Med 25, 270–276 (2019). [PubMed: 30643288]

51. Foo SS et al. Ephrin-B2 controls cell motility and adhesion during blood-vessel-wall assembly. Cell 124, 161–173 (2006). [PubMed: 16413489]

52. Zhu X, Bergles DE & Nishiyama A NG2 cells generate both oligodendrocytes and gray matter astrocytes. Dev. Camb. Engl 135, 145–157 (2008).

53. Sharan SK, Thomason LC, Kuznetsov SG & Court DL Recombineering: a homologous recombination-based method of genetic engineering. Nat. Protoc 4, 206–223 (2009). [PubMed: 19180090]

54. Nikolakopoulou AM et al. Astrocytic Ephrin-B1 Regulates Synapse Remodeling Following Traumatic Brain Injury. ASN Neuro 8, 1–18 (2016). [PubMed: 26928051]

55. Li G-W, Burkhardt D, Gross C & Weissman JS Quantifying absolute protein synthesis rates reveals principles underlying allocation of cellular resources. Cell 157, 624–635 (2014). [PubMed: 24766808]

56. Wu Z, Hofman FM & Zlokovic BV A simple method for isolation and characterization of mouse brain microvascular endothelial cells. J. Neurosci. Methods 130, 53–63 (2003). [PubMed: 14583404]

57. Ruck T, Bittner S, Epping L, Herrmann AM & Meuth SG Isolation of Primary Murine Brain Microvascular Endothelial Cells. J. Vis. Exp (2014). doi:10.3791/52204

58. Zhao Z et al. Central role for PICALM in amyloid-β blood-brain barrier transcytosis and clearance. Nat. Neurosci 18, 978–987 (2015). [PubMed: 26005850]

59. Bell RD et al. SRF and myocardin regulate LRP-mediated amyloid-beta clearance in brain vascular cells. Nat. Cell Biol 11, 143–153 (2009). [PubMed: 19098903]

60. Gauthier SA, Sahoo S, Jung SS & Levy E Murine cerebrovascular cells as a cell culture model for cerebral amyloid angiopathy: isolation of smooth muscle and endothelial cells from mouse brain. Methods Mol. Biol. Clifton NJ 849, 261–274 (2012).

61. Zhong Z et al. Protein S protects neurons from excitotoxic injury by activating the TAM receptor Tyro3-phosphatidylinositol 3-kinase-Akt pathway through its sex hormone-binding globulin-like region. J. Neurosci. Off. J. Soc. Neurosci 30, 15521–15534 (2010).

62. Schildge S, Bohrer C, Beck K & Schachtrup C Isolation and Culture of Mouse Cortical Astrocytes. J. Vis. Exp (2013). doi:10.3791/50079

63. Trost A et al. Neural crest origin of retinal and choroidal pericytes. Invest. Ophthalmol. Vis. Sci 54, 7910–7921 (2013). [PubMed: 24235018]

64. Nikolakopoulou AM, Zhao Z, Montagne A & Zlokovic BV Regional early and progressive loss of brain pericytes but not vascular smooth muscle cells in adult mice with disrupted platelet-derived growth factor receptor-β signaling. PloS One 12, e0176225 (2017). [PubMed: 28441414]

65. Victor MB et al. Generation of human striatal neurons by microRNA-dependent direct conversion of fibroblasts. Neuron 84, 311–323 (2014). [PubMed: 25374357]

66. Chen K et al. Synergic interaction between amyloid precursor protein and neural cell adhesion molecule promotes neurite outgrowth. Oncotarget 7, 14199–14206 (2016). [PubMed: 26883101]

67. Winkler EA et al. GLUT1 reductions exacerbate Alzheimer's disease vasculo-neuronal dysfunction and degeneration. Nat. Neurosci 18, 521–530 (2015). [PubMed: 25730668]

68. Iadecola C et al. SOD1 rescues cerebral endothelial dysfunction in mice overexpressing amyloid precursor protein. Nat. Neurosci 2, 157–161 (1999). [PubMed: 10195200]

69. Park L, Anrather J, Girouard H, Zhou P & Iadecola C Nox2-derived reactive oxygen species mediate neurovascular dysregulation in the aging mouse brain. J. Cereb. Blood Flow Metab. Off. J. Int. Soc. Cereb. Blood Flow Metab 27, 1908–1918 (2007).

70. Barnes SR et al. ROCKETSHIP: a flexible and modular software tool for the planning, processing and analysis of dynamic MRI studies. BMC Med. Imaging 15, 19 (2015). [PubMed: 26076957]

71. Montagne A et al. Blood-Brain Barrier Breakdown in the Aging Human Hippocampus. Neuron 85, 296–302 (2015). [PubMed: 25611508]

72. Barnes SR et al. Optimal acquisition and modeling parameters for accurate assessment of low Ktrans blood-brain barrier permeability using dynamic contrast-enhanced MRI. Magn. Reson. Med 75, 1967–1977 (2016). [PubMed: 26077645]

73. Ostergaard L, Weisskoff RM, Chesler DA, Gyldensted C & Rosen BR High resolution measurement of cerebral blood flow using intravascular tracer bolus passages. Part I: Mathematical approach and statistical analysis. Magn. Reson. Med 36, 715–725 (1996). [PubMed: 8916022]

74. Jiang H, van Zijl PCM, Kim J, Pearlson GD & Mori S DtiStudio: Resource program for diffusion tensor computation and fiber bundle tracking. Comput. Methods Programs Biomed 81, 106–116 (2006). [PubMed: 16413083]

75. Kimura R, Devi L & Ohno M Partial reduction of BACE1 improves synaptic plasticity, recent and remote memories in Alzheimer's disease transgenic mice. J. Neurochem 113, 248–261 (2010). [PubMed: 20089133]

76. Sweatt JD Rodent Behavioral Learning and Memory Models in Mechanisms of Memory 76–103 (Elsevier, 2010). doi:10.1016/B978-0-12-374951-2.00004-4

77. Mazziotti R et al. Mir-132/212 is required for maturation of binocular matching of orientation preference and depth perception. Nat. Commun 8, 15488 (2017). [PubMed: 28534484]

78. Kisler K et al. In vivo imaging and analysis of cerebrovascular hemodynamic responses and tissue oxygenation in the mouse brain. Nat. Protoc 13, 1377–1402 (2018). [PubMed: 29844521]

79. Zhu D et al. Protein S controls hypoxic/ischemic blood-brain barrier disruption through the TAM receptor Tyro3 and sphingosine 1-phosphate receptor. Blood 115, 4963–4972 (2010). [PubMed: 20348395]

80. Wang Y et al. An activated protein C analog with reduced anticoagulant activity extends the therapeutic window of tissue plasminogen activator for ischemic stroke in rodents. Stroke 43, 2444–2449 (2012). [PubMed: 22811462]

81. Guo H et al. Activated protein C prevents neuronal apoptosis via protease activated receptors 1 and 3. Neuron 41, 563–572 (2004). [PubMed: 14980205]
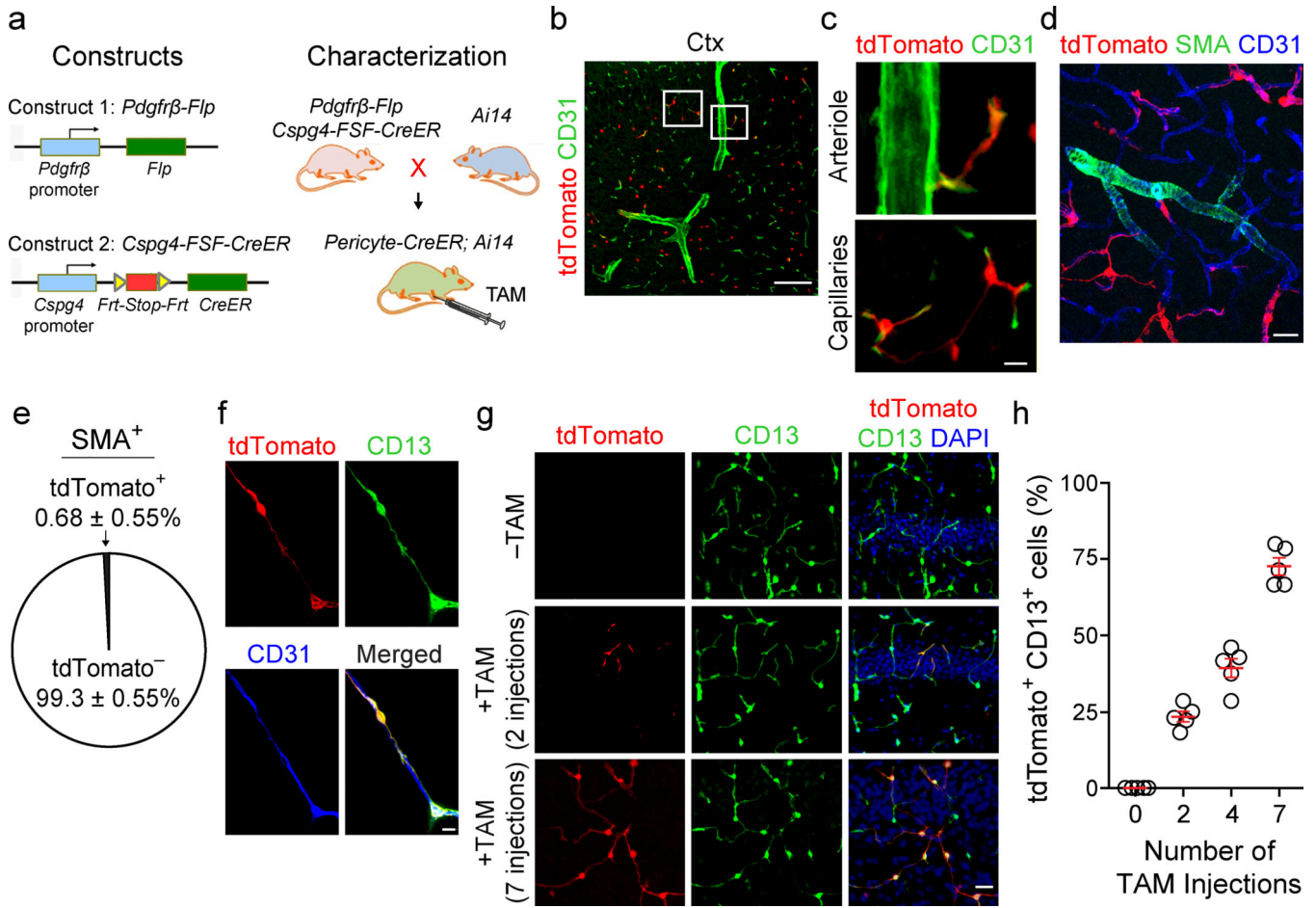
Figure 1. Generation of a pericyte-specific Cre line.
(**a**) Constructs: *Pdgfrb* promoter expressing Flippase (Flp) and *Cspg4* promoter driving the *Frt-Stop-Frt-CreER* cassette. Crossing: *Pdgfrβ-Flp; Cspg4-FSF-CreER* mice X Ai14 tdTomato line. (**b-f**) Characterization of pericyte-specific Cre line with the Ai14 reporter mice. **b**, Expression of tdTomato in perivascular cells in the cortex 1 week after tamoxifen (TAM) (4 injections 40 mg/kg daily). Bar = 50 μm. **c**, Representative images from the boxed regions in **b**, showing restricted expression of tdTomato in perivascular cells of brain capillaries. **d**, tdTomato expression on brain capillaries, but not on arteriolar vascular smooth muscle cells. SMA, α-smooth muscle actin. **e**, SMA+ tdTomato+ and SMA+ tdTomato- cells in the cortex; Mean ± S.E.M., n = 55 mice. **f**, Colocalization of tdTomato with pericyte marker CD13 (green). CD31, endothelial marker. Bar = 10 μm. (**g,h**) Representative images (**g**) and quantification (**h**) of pericytes expressing tdTomato (%) plotted against the number of TAM injections (40 mg/kg daily). DAPI, nuclear staining. In **h**, significant increase in tdTomato+ CD13+ cells (%) at 2 vs. 0 TAM injections ($P = 9.5E^{-6}$), at 4 vs. 2 TAM injections ($P = 7.6E^{-4}$), and at 7 vs. 4 TAM injections ($P = 8.5E^{-8}$); Mean ± S.E.M., n = 5 mice/group. Significance by one-way ANOVA followed by Bonferroni posthoc test. Bars = 20 μm, panels **c**, **d** and **g**. Experiments illustrated in panels b-d, f, and g were repeated independently with similar results in 5 mice.
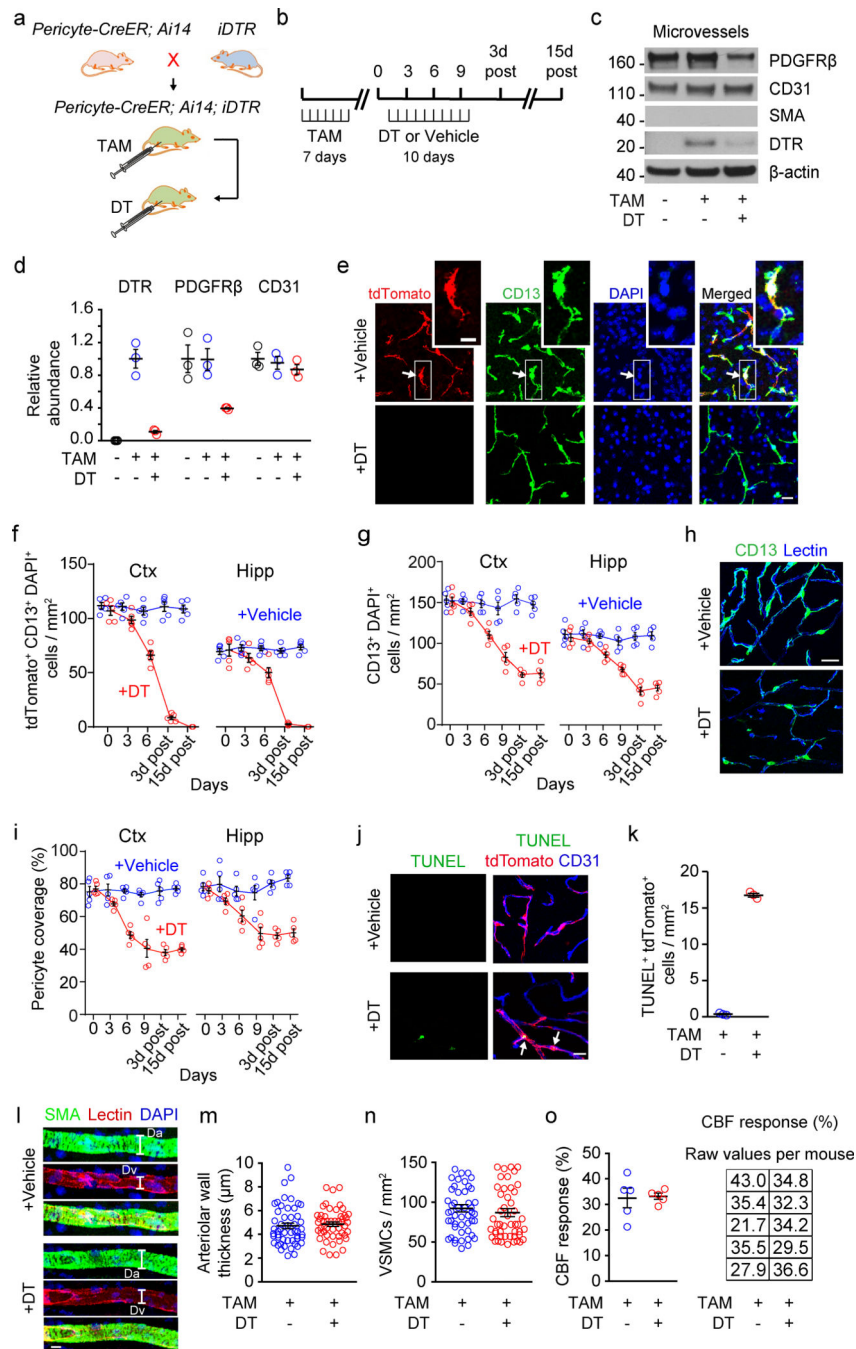
Figure 2. Pericyte ablation with diphtheria toxin.
(**a**) Breeding: Pericyte-CreER; Ai14 X iDTR mice. (**b**) A diagram of the injection protocol with TAM (40 mg/kg daily for 7 consecutive days), DT (0.1 μg per day for 10 consecutive days beginning two weeks after TAM) or vehicle, and time points when analyses were performed. (**c,d**) Immunoblotting (**c**) and quantification (**d**) of DTR, PDGFRβ, and CD31 in brain microvessels from TAM-treated pericyte-CreER; iDTR mice at 3 days post-DT or vehicle. In TAM + DT-treated mice compared to TAM + vehicle-treated control mice, relative microvascular abundance of DTR and PDGFRβ was significantly decreased ($P =$

$2.6E^{-4}$ and $P = 4E^{-2}$, respectively), whereas relative abundance of CD31 was unchanged ($P = 0.49$). Mean ± S.E.M., n = 3 mice/group. PDGFRβ, pericyte marker; CD31, endothelial marker; SMA, α-smooth muscle cell actin; DTR, DT receptor. (**e-g**) tdTomato, CD13 and DAPI staining in the cortex 3 days post-DT or vehicle (**e**) and quantification of tdTomato+ CD13+ DAPI+ pericytes (**f**) and CD13+ DAPI+ pericytes (**g**) in the cortex (Ctx) and hippocampus (Hipp) of TAM-treated pericyte-CreER; Ai14; iDTR mice at 0, 3, 6 and 9 days of DT, and 3 and 15 days post-DT or vehicle. Mean ± S.E.M., n = 5 mice/group. In **e**, white in merged image indicates colocalization of tdTomato, CD13 and DAPI (white arrows), and is representative of staining repeated independently with similar results in 5 mice. Bar = 20 μm. Inset bar = 10 μm. In **f**, DT-treated mice compared to vehicle-treated mice had significantly less tdTomato+ CD13+ DAPI+ cells in Ctx at day 6 of treatment ($P = 7E^{-9}$), 3 days post-treatment ($P = 1E^{-15}$), and 15 days post-treatment ($P = 1E^{-15}$); and, significantly less tdTomato+ CD13+ DAPI+ cells in Hipp at day 6 of treatment ($P = 5.6E^{-4}$), 3 days post-treatment ($P = 1E^{-15}$), and 15 days post-treatment ($P = 1E^{-15}$). In **g**, DT-treated mice compared to vehicle-treated mice had significantly less CD13+ DAPI+ cells in Ctx at day 6 of treatment ($P = 1E^{-4}$), day 9 of treatment ($P = 3E^{-9}$), 3 days post-treatment ($P = 1E^{-15}$), and 15 days post-treatment ($P = 3E^{-14}$); and, significantly less CD13+ DAPI+ cells in Hipp at day 6 of treatment ($P = 2E^{-2}$), day 9 of treatment ($P = 2E^{-5}$), 3 days post-treatment ($P = 3E^{-13}$), and 15 days post-treatment ($P = 9E^{-13}$). (**h,i**) CD13+ pericyte coverage of lectin+ endothelial profiles in the cortex 3 days post-DT or vehicle (**h**; Bar = 20 μm), and quantification of pericyte coverage on capillaries (<6 μm in diameter) in Ctx and Hipp (**i**) in TAM-treated pericyte-CreER; iDTR mice at 0, 3, 6 and 9 days of DT, and 3 and 15 days post-DT or vehicle. Mean ± S.E.M., n = 5 mice/group. In **i**, DT-treated mice compared to vehicle-treated mice had significantly less capillary pericyte coverage in Ctx at day 6 of treatment ($P = 8E^{-8}$), day 9 of treatment ($P = 3E^{-10}$), 3 days post-treatment ($P = 3E^{-12}$), and 15 days post-treatment ($P = 5E^{-12}$); and, significantly less capillary pericyte coverage in Hipp at day 6 of treatment ($P = 4.7E^{-2}$), day 9 of treatment ($P = 1.8E^{-5}$), 3 days post-treatment ($P = 5.7E^{-8}$), and 15 days post-treatment ($P = 1.5E^{-8}$). (**j,k**) Representative images (**j**) and quantification (**k**) of TUNEL+ tdTomato+ pericytes on CD31+ endothelial profiles in the cortex of TAM-treated pericyte CreER; iDTR; Ai14 mice at 6 days of treatment with DT compared to vehicle ($P = 5E^{-7}$). Arrows, TUNEL+ tdTomato+ cells. Bar = 20 μm. Mean ± S.E.M., n = 3 mice/group. (**l**) SMA+ vascular smooth muscle cells (VSMCs) (green, top), lectin+ endothelial profiles (red, middle), and merged (bottom) in penetrating arterioles in the cortex of TAM-treated pericyte-CreER; iDTR mice 3 days post-DT or vehicle, representative of 50 independent arterioles with similar results from 5 mice per condition. Da, SMA+ arteriolar diameter; Dv, lectin+ endothelial diameter. Bar = 20 μm. (**m-o**) Arteriolar wall thickness (**m**, $P = 0.37$), VSMCs number (**n**, $P = 0.46$) and cerebral blood flow (CBF) response to adenosine by laser Doppler flowmetry (**o**, $P = 0.84$) in TAM-treated pericyte-CreER; iDTR mice 3 days post-DT compared to vehicle treatment. Mean ± S.E.M.; n = 5 mice/group; ns, non-significant. In **m** and **n**, individual points are 10 vessels/mouse from n = 5 mice/group. Mean ± S.E.M. from 50 arterioles/group. ns, non-significant. Significance by one-way ANOVA followed by Bonferroni posthoc test in **d**, **f**, **g**, and **i**, and two-tail Student's t-test in **k**, **m**, **n** and **o**. See Supplementary Figure 11 for full scans of Western blots used for quantification in **c**.
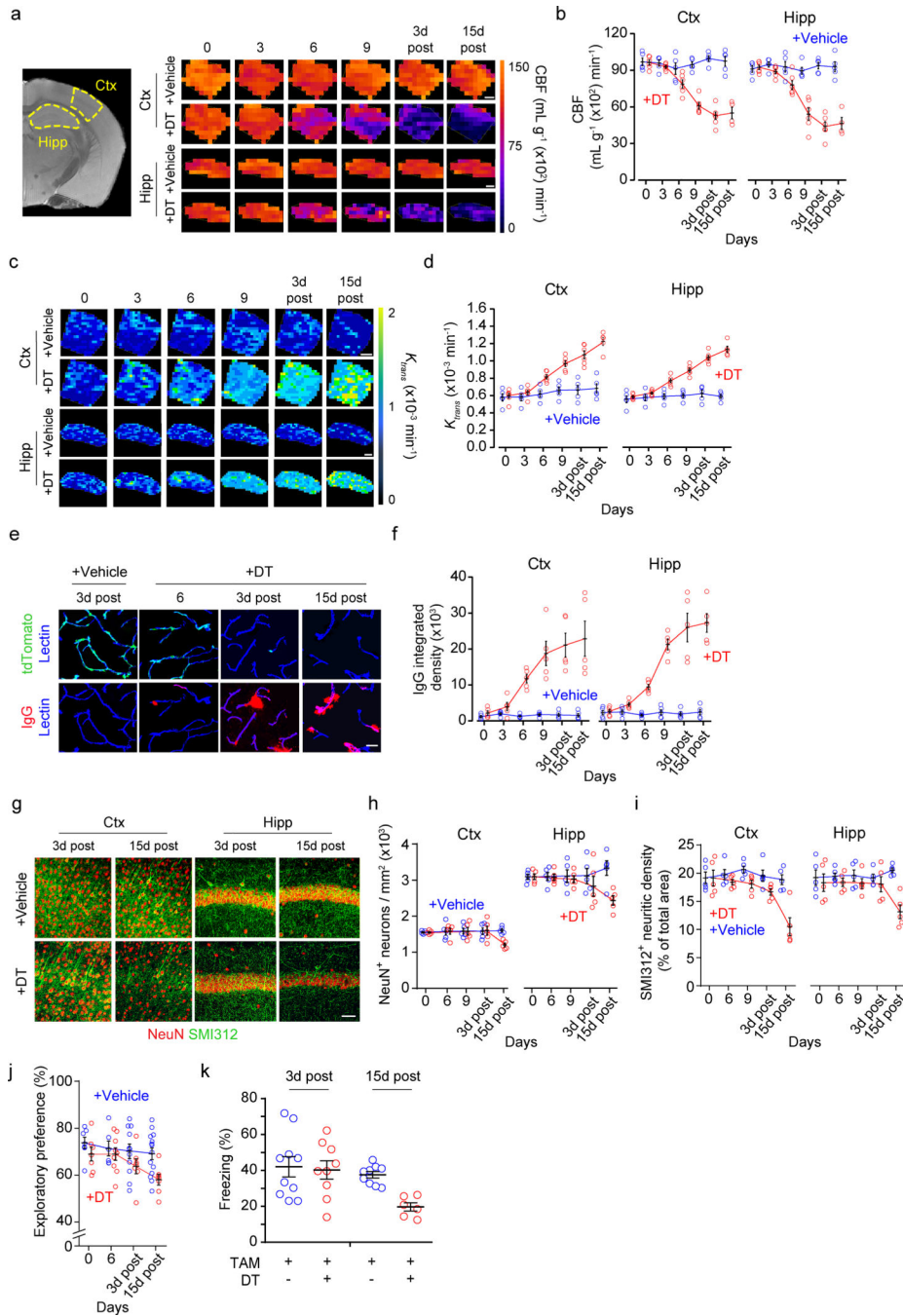
Figure 3. Acute circulatory failure and rapid neuron loss after pericyte ablation.
(**a,b**) Cerebral blood flow (CBF) maps (**a**) and regional CBF values in the primary somatosensory cortex (Ctx) and hippocampus (Hipp) (**b**) of TAM-treated pericyte-CreER; iDTR mice at 0, 3, 6, and 9 days of DT, and 3 and 15 days post-DT (red) or vehicle (blue) generated by dynamic susceptibility-contrast MRI with gadolinium. Images are representative (**a**), and quantified (**b**) from n = 5 vehicle-treated and 6 DT-treated independent mice/group at 0, 3, 6, and 9 days of DT and 3 days post-DT, and n = 5 vehicle-treated and 4 DT-treated independent mice/group at 15 days post-DT. In **a**, bar = 0.5 mm. In

b, DT-treated mice compared to vehicle-treated mice had significantly reduced CBF in Ctx at day 9 of treatment ($P = 1E^{-8}$), 3 days post-treatment ($P = 2E^{-13}$), and 15 days post-treatment ($P = 2E^{-10}$); and, had significantly reduced CBF in Hipp at day 9 of treatment ($P = 8.5E^{-8}$), 3 days post-treatment ($P = 2.2E^{-12}$), and 15 days post-treatment ($P = 7E^{-10}$). (**c,d**) Unidirectional transfer constant (K_{trans}) blood-brain barrier maps to intravenous gadolinium in Ctx and Hipp (**c**) and regional K_{trans} values in Ctx and Hipp (**d**) of TAM-treated pericyte-CreER; iDTR mice at 0, 3, 6, and 9 days of DT, and 3 and 15 days post-DT (red) or vehicle (blue) generated by longitudinal dynamic contrast-enhanced MRI. Images are representative (**c**) and quantified (**d**) from n = 5 vehicle-treated and 6 DT-treated independent mice/group at 0, 3, 6, and 9 days of DT and 3 days post-DT, and n = 5 vehicle-treated and 5 DT-treated independent mice/group at 15 days post-DT. In **c**, bar = 0.5 mm. In **d**, DT-treated mice compared to vehicle-treated mice had significantly increased K_{trans} values in Ctx at day 6 of treatment ($P = 5.5E^{-2}$), day 9 of treatment ($P = 6.6E^{-5}$), 3 days post-treatment ($P = 1E^{-7}$), and 15 days post-treatment ($P = 6.2E^{-11}$); and, had significantly increased K_{trans} values in Hipp at day 6 of treatment ($P = 1.8E^{-3}$), day 9 of treatment ($P = 5E^{-8}$), 3 days post-treatment ($P = 6.7E^{-13}$), and 15 days post-treatment ($P = 1E^{-15}$). In **b** and **d**, data is Mean ± S.E.M. (**e,f**) Immunoglobulin G perivascular deposits (red) in cortex (**e**) and quantification of IgG deposits in Ctx and Hipp (**f**) of TAM-treated pericyte-CreER; Ai14; iDTR mice at 0, 3, 6 and 9 days of DT, and 3 and 15 days post-DT or vehicle. Blue, lectin+ endothelial profiles; green, tdTomato+ pericytes. Bar = 20 μm. Mean ± S.E.M., n = 5 mice/group. In **f**, DT-treated mice compared to vehicle-treated mice had significantly increased IgG perivascular deposits in Ctx at day 6 of treatment ($P = 4.7E^{-2}$), day 9 of treatment ($P = 2.6E^{-5}$), 3 days post-treatment ($P = 1.4E^{-6}$), and 15 days post-treatment ($P = 1.4E^{-7}$); and, had significantly increased IgG perivascular deposits in Hipp at day 6 of treatment ($P = 4.9E^{-2}$), day 9 of treatment ($P = 1.2E^{-9}$), 3 days post-treatment ($P = 4.7E^{-13}$), and 15 days post-treatment ($P = 1.5E^{-13}$). (**g-i**) NeuN+ neurons (red, **g**) and SMI312+ neurofilaments (green, **g**) in Ctx and Hipp of TAM-treated pericyte-CreER; iDTR mice 3 and 15 days post-DT or vehicle, and quantification of NeuN+ neurons (**h**) and SMI312+ neuritic density (**i**) during and post-DT or vehicle treatment. Bar = 20 μm. Mean ± S.E.M., n = 5 mice/group. In **h**, DT-treated mice compared to vehicle-treated mice had significantly reduced numbers of NeuN+ neurons in Ctx ($P = 4.4E^{-2}$) and Hipp ($P = 1.1E^{-2}$) at 15 days post-treatment. In **i**, DT-treated mice compared to vehicle-treated mice had significantly reduced SMI312+ neuritic density in Ctx ($P = 2.1E^{-5}$) and Hipp ($P = 5.6E^{-4}$) at 15 days post-treatment. (**j,k**) Novel object location (**j**) and fear conditioning (**k**) in TAM-treated pericyte-CreER; iDTR mice at 0 and 6 days of DT (**j**), and 3 and 15 days post-DT or vehicle (**j,k**). DT-treated mice compared to vehicle-treated mice had significantly reduced exploratory preference (**j**, $P = 2.4E^{-2}$) and performance on fear conditioning (**k**, $P = 2.9E^{-2}$) at 15 days post-treatment. Mean ± S.E.M. In **j**, n = 7 vehicle-treated and 7 DT-treated mice/group at 0 days DT; n = 6 vehicle-treated, 9 DT-treated mice/group at 6 days DT; n = 11 vehicle-treated, 7 DT-treated mice/group at 3 days post-DT; n = 14 vehicle-treated, 7 DT-treated mice/group at 15 days post-DT. In **k**, n = 10 vehicle-treated, 9 DT-treated mice/group at 3 days post-DT; n = 9 vehicle-treated, 6 DT-treated mice/group at 15 days post-DT. In **b**, **d**, **f**, **h**, **i**, **j** and **k**, significance by one-way ANOVA followed by Bonferroni posthoc test.
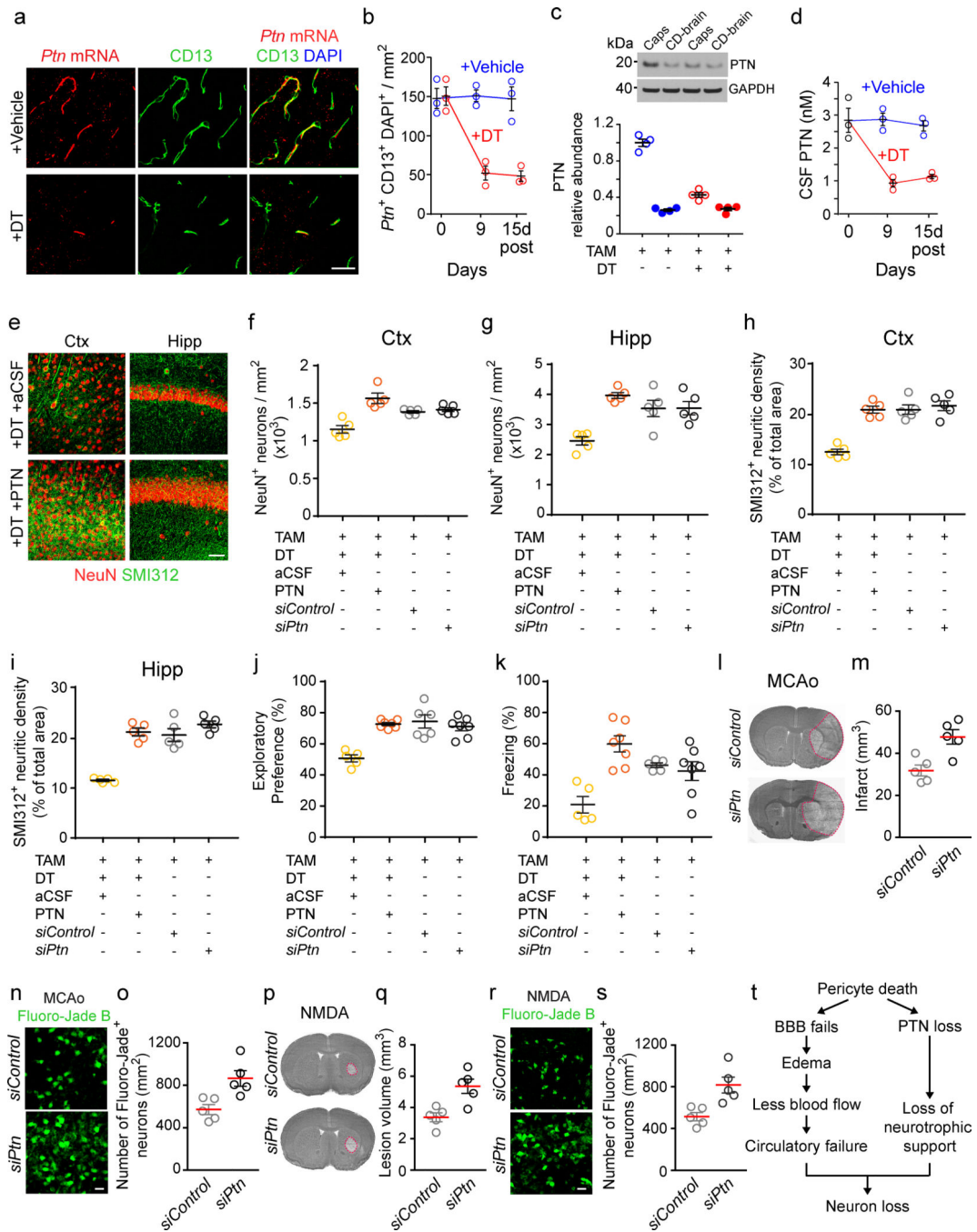
Figure 4. Loss of pericyte-derived pleiotrophin (PTN)-mediated neuroprotection.
(**a,b**) Dual fluorescent *in situ* hybridization for *Ptn* mRNA and immunostaining for CD13+ pericytes in cortex of TAM-treated pericyte-CreER; iDTR mice at 15 days post-DT or vehicle (**a**, representative of 3 independent mice/group with similar results), and quantification (**b**) of *Ptn*+ CD13+ DAPI+ pericytes at 0 and 9 days of DT, and 15 days post-DT or vehicle. Bar = 40 μm. In **b**, DT-treated mice compared to vehicle-treated mice had significantly less *Ptn*+ CD13+ DAPI+ pericytes at day 9 of treatment ($P = 5E^{-4}$) and 15 days post-treatment ($P = 5E^{-4}$). (**c,d**) PTN expression in capillaries (Caps) and capillary-depleted

brain (CD-brain) (**c**) and cerebrospinal fluid (CSF) PTN levels in TAM-treated pericyte-CreER; iDTR mice (**d**) at 0 and 9 days of DT, and 15 days post-DT or vehicle. In **c**, PTN relative capillary abundance was significantly decreased in TAM + DT-treated mice compared to TAM + vehicle-treated mice ($P = 2E^{-8}$). In **d**, TAM + DT-treated mice compared to TAM + vehicle-treated mice had significantly reduced CSF PTN levels at day 9 of treatment ($P = 5.4E^{-4}$) and 15 days post-treatment ($P = 3.3E^{-3}$). In **b-d**, Mean ± S.E.M., n = 3 mice/group. (**e-i**) NeuN+ neurons (red, **e**) and SMI312+ neurofilaments (green, **e**) in Ctx and Hipp of TAM-treated pericyte-CreER; iDTR mice receiving DT for 10 days and PTN or artificial CSF (aCSF) by intracerebroventricular (ICV) bilateral infusion (from day 6 of DT to 15 days post-DT), and quantification of NeuN+ neurons (**f,g**) and SMI312+ neuritic density (**h,i**) in Ctx and Hipp after PTN and aCSF infusion compared to 2 weeks post-si*Ptn* or si*Control* (scrambled siRNA) ICV treatment of TAM-treated pericyte-CreER; iDTR mice receiving vehicle. Mean ± S.E.M., n = 5 mice/group. In **e**, Bar = 20 μm. In **f**, TAM + DT + PTN-treated mice compared to TAM + DT + aCSF-treated mice had significantly increased number of NeuN+ neurons in Ctx ($P = 1.7E^{-5}$), whereas TAM + si*Ptn*-treated mice compared to TAM + si*Control*-treated mice showed no difference ($P = 0.99$). In **g**, TAM + DT + PTN-treated mice compared to TAM + DT + aCSF-treated mice had significantly increased number of NeuN+ neurons in Hipp ($P = 3E^{-4}$), whereas TAM + si*Ptn*-treated mice compared to TAM + si*Control*-treated mice showed no difference ($P = 0.99$). In **h**, TAM + DT + PTN-treated mice compared to TAM + DT + aCSF-treated mice had significantly increased SMI312+ neuritic density in Ctx ($P = 9E^{-6}$), whereas TAM + si*Ptn*-treated mice compared to TAM + si*Control*-treated mice showed no difference ($P = 0.99$). In **i**, TAM + DT + PTN-treated mice compared to TAM + DT + aCSF-treated mice had significantly increased SMI312+ neuritic density in Hipp ($P = 2.1E^{-6}$), whereas TAM + si*Ptn*-treated mice compared to TAM + si*Control*-treated mice showed no difference ($P = 0.53$). (**j,k**) Novel object location (**j**) and fear conditioning (**k**) in TAM-treated pericyte-CreER; iDTR mice receiving DT for 10 days and PTN or aCSF ICV infusions at 15 days post-DT, or 2 weeks after si*Ptn* or si*Control* ICV treatment of TAM-treated pericyte-CreER; iDTR mice. Mean ± S.E.M., n = 5 DT + aCSF, 7 DT + PTN, 7 si*Ptn* and 6 si*Control* (**j**) or 5 si*Control* (**k**) mice/group. In **j**, TAM + DT + PTN-treated mice compared to TAM + DT + aCSF-treated mice had significantly increased exploratory preference ($P = 3.9E^{-5}$), whereas TAM + si*Ptn*-treated mice compared to TAM + si*Control*-treated mice showed no difference ($P = 0.99$). In **k**, TAM + DT + PTN-treated mice compared to TAM + DT + aCSF-treated mice had significantly increased performance on fear conditioning ($P = 2.5E^{-4}$), whereas TAM + si*Ptn*-treated mice compared to TAM + si*Control*-treated mice showed no difference ($P = 0.99$). (**l-s**) Injury volume and fluoro-jade+ degenerating neurons in mice treated with si*Ptn* or si*Control* challenged by a transient middle cerebral artery occlusion (MCAo) stroke (**l-o**) or N-methyl-D-aspartate (NMDA) excitotoxic lesions (**p-s**). Mean ± S.E.M., n = 5 mice/group. Bar = 20 μm in **n** and **r**. In **m** and **o**, si*Ptn*-treated mice compared to si*Control*-treated mice had larger infarcts (**m**, $P = 5.9E^{-3}$) and increased number of Fluoro-Jade+ neurons (**o**, $P = 9.7E^{-3}$). In **q** and **s**, si*Ptn*-treated mice compared to si*Control*-treated mice had larger lesion volume (**q**, $P = 6.1E^{-3}$) and increased number of Fluoro-Jade+ neurons (**s**, $P = 7.8E^{-3}$). (**t**) Neurodegeneration cascade linking pericyte loss to neuron loss. Significance by one-way ANOVA followed by Bonferroni posthoc test in **b-d**, **f-k**, and two-tail Student's t-test in

m, **o**, **q**, **s**. See Supplementary Figure 11 for full scans of Western blots used for quantification in **c**.